Accepted manuscript (author version)

To appear in:

Iranian Journal of Catalysis (IJC)

Online ISSN: 2345-4865 Print ISSN: 2252-0236

Received: 24 November 2025

Revised: 06 January 2026

Accepted: 08 February 2026

Published Online: 18 May 2026

DOI: 10.57647/ijc.2026.1602.16

RESEARCH PAPER

Synthesis of Magnetic Mesoporous Fe_3O_4@SB Nanocomposite Adsorbent for Efficient Removal of Pharmaceutical Active Compounds from Water Solution

Somayyeh Shenavaie asl[a], Afshin Pourahmad[a,*], Somayyeh Rostamzadeh Mansour[b], and Nastaran Sohrabi-Gilani[b]

[a] *Department of Chemistry, Ra. C., Islamic Azad University, Rasht, Iran*
[b] *Department of Chemistry, Ard. C., Islamic Azad University, Ardebil, Iran*
* Corresponding author email: *pourahmad@iau.ac.ir*

ORCIDs:
Somayyeh Shenavaie asl : https://orcid.org/0009-0002-7527-6776
Afshin Pourahmad : https://orcid.org/0000-0003-2007-8991
Somayyeh Rostamzadeh Mansour : https://orcid.org/0000-0003-2487-0978
Nastaran Sohrabi-Gilani : https://orcid.org/0009-0008-5587-8087

Abstract:
This study reports the successful synthesis of a novel magnetic nanocomposite, Fe_3O_4@SB, for the efficient removal of pharmaceutical active compounds (PhACs) from water. The material was fabricated by grafting a robust, mesoporous Schiff base (SB) network onto superparamagnetic Fe_3O_4 nanoparticles. The adsorption performance was evaluated for three model pharmaceuticals: 5-fluorouracil, mefenamic acid, and tryptophan. Under optimized conditions, the Fe_3O_4@SB nanocomposite exhibited exceptional removal efficiencies exceeding 96% for all compounds, with remarkably rapid kinetics reaching equilibrium within 10–15 min. Adsorption isotherm analysis revealed that the process followed the Langmuir model, indicating monolayer adsorption, with high maximum capacities for PhACs. Furthermore, the nanocomposite demonstrated excellent reusability over five consecutive adsorption-desorption cycles with minimal loss in capacity. The combination of high efficiency, rapid kinetics, facile magnetic separation, and robust stability positions Fe_3O_4@SB as a highly promising and practical adsorbent for the remediation of pharmaceutical-contaminated water.

Keywords: Adsorption; Fe_3O_4; Magnetic nanocomposite; Pharmaceutical active compounds (Phuc's); Schiff base; Water treatment

1. Introduction

The escalating contamination of global water resources by pharmaceutical active compounds (places) represents a critical environmental challenge of the 21st century. These persistent micropollutants, originating from widespread domestic use, industrial discharge, and agricultural runoff, are continually introduced into aquatic systems and often bypass conventional wastewater treatment processes [1, 2]. Their presence, even at trace concentrations (ng L^{-1} to µg L^{-1}), poses potential risks to aquatic ecosystems and human health, including the development of antibiotic-resistant bacteria and endocrine disruption [3, 4]. Among the myriad of places, compounds such as the non-steroidal anti-inflammatory drug mefenamic acid (MA), the essential amino acid tryptophan (TRP), and the anticancer agent 5-fluorouracil (5-FU) are frequently detected, necessitating the development of advanced remediation technologies for their efficient removal [5]. Tryptophan was included in this study as a pharmaceutical active compound (PhAC) due to its widespread use as a therapeutic supplement and precursor in pharmaceutical formulations. Although tryptophan is an essential amino acid, it is frequently administered in high doses as a nutraceutical or drug component, and its release into aquatic environments through pharmaceutical effluents has been reported. Therefore, for the purpose of evaluating adsorption behavior toward structurally diverse bioactive compounds, tryptophan was categorized alongside mefenamic acid and 5-fluorouracil.

In response to this imperative, adsorption has emerged as a prominent and effective technique, prized for its operational simplicity, cost-effectiveness, and high efficiency [6]. The quest for superior adsorbents has led researchers to explore advanced materials, with magnetic nanocomposites garnering significant attention. The integration of superparamagnetic iron oxide nanoparticles (e.g., Fe_3O_4) into adsorbent frameworks facilitates rapid magnetic separation post-treatment, eliminating the need for energy-intensive centrifugation or filtration, thereby enhancing process practicality and economic viability [7-10]. However, pristine magnetic nanoparticles suffer from inherent limitations, including aggregation, oxidative instability, and a lack of specific binding sites, which curtail their adsorption capacity and reusability [11].

To overcome these drawbacks, surface engineering of magnetic cores with porous functional materials has become a cornerstone of advanced adsorbent design. In particular, covalent organic frameworks (COFs) and related porous polymers, constructed from organic building blocks via robust covalent bonds, offer an attractive platform due to their high surface areas, tunable pore architectures, and abundant functional groups [12, 13]. Schiff base (SB) chemistry, which involves the condensation of amines and aldehydes to form imine linkages, provides a versatile route for directly constructing such functional networks on nanoparticle surfaces, thereby creating a synergistic composite [14]. These coatings not only prevent nanoparticle aggregation but also introduce specific interaction sites such as aromatic rings for π-π stacking and nitrogen/oxygen atoms for hydrogen bonding tailored for the selective capture of diverse organic pollutants [15, 16].

Recent literature underscores the efficacy of such magnetic COF composites. For instance, you et al. demonstrated that a Fe_3O_4@COF material exhibited high adsorption capacity for bisphenols, attributing the performance to π-π and hydrogen bonding interactions [17]. Similarly, Wang et al. developed a magnetic COF for mycotoxin extraction, highlighting the importance of the mesoporous structure for accommodating target analytes [18]. Very recently, Zhang et al. synthesized a novel magnetic covalent organic framework for the extraction of macrolide antibiotics, demonstrating the continuous innovation in this field [19]. Despite these advancements, a research gap remains in developing easily synthesized, magnetically separable adsorbents that demonstrate rapid kinetics and high capacity for a broad spectrum of PhACs with differing ionic character, all while maintaining structural stability over multiple cycles.

This work addresses the identified gap by reporting the facile one-pot synthesis and application of a novel magnetic mesoporous nanocomposite, Fe_3O_4@SB, engineered for the rapid and efficient removal of three model places with divergent ionic character: MA (acidic), TRP (amphoteric), and 5-FU (neutral/basic). The novelty and key advantages of this work are fourfold:

(1). *Material innovation*: We present a straightforward and scalable synthesis route that directly grafts a robust, mesoporous Schiff base (SB) network onto superparamagnetic Fe_3O_4 nanoparticles via a silane linker. This design integrates the high magnetic susceptibility of magnetite with the tunable porosity and abundant functional groups of Schiff base polymers in a single, stable composite.

(2). *Performance excellence*: The resulting Fe_3O_4@SB nanocomposite demonstrates exceptional and rapid adsorption performance, achieving >96% removal for all three target PhACs with remarkably fast kinetics (equilibrium within 10–15 min), a significant operational advantage over many slower adsorbents.

(3). *Practical superiority*: The material exhibits excellent reusability over multiple cycles and, crucially, enables instantaneous, energy-efficient magnetic separation post-treatment. This combination of high efficiency, rapid operation, and facile recovery directly addresses practical and economic imperatives for real-world water treatment.

(4). *Mechanistic clarity*: Through systematic study including determination of the point of zero charge (pHpzc), we provide a comprehensive, evidence-based mechanistic interpretation that decouples the roles of π-π stacking, hydrogen bonding, and electrostatic interactions in the adsorption process for each pharmaceutical.

The primary objectives of this study are therefore to: (i) comprehensively characterize the structural, morphological, textural, and magnetic properties of the synthesized Fe_3O_4@SB; (ii) evaluate its adsorption performance against MA, TRP, and 5-FU under varying operational parameters (pH, contact time, adsorbent dosage); (iii) elucidate the adsorption kinetics, isotherms, and the underlying interaction mechanisms; and (iv) assess the reusability and stability of the nanocomposite. The demonstrated performance positions Fe_3O_4@SB not merely as another adsorbent, but as a highly promising,

practical, and versatile candidate for the remediation of pharmaceutical-contaminated water streams.

2. Experiment and method

2.1. Materials

All chemicals and reagents employed in this study were of analytical grade and were used as received without further purification. Iron (II) chloride tetrahydrate ($FeCl_2.4H_2O$) and iron(III) chloride hexahydrate ($FeCl_3.6H_2O$) served as precursors for the co-precipitation synthesis of magnetite nanoparticles (Fe_3O_4). A 25% ammonia solution (NH_3) was used to adjust the pH during the synthesis. The target pharmaceutical active compounds (PhACs) were used as pure analytical standards: mefenamic acid (MA, ≥98% purity), L-tryptophan (TRP, ≥99% purity), and 5-fluorouracil (5-FU, ≥99% purity). All standards were supplied by Cedal Nano Pharmaceutical Company (Iran) and were used as received without further purification. Dilute solutions of sodium hydroxide (NaOH) and hydrochloric acid (HCl) were utilized for pH adjustments throughout the adsorption experiments. Ethanol and distilled water were used for all cleaning and purification procedures. Unless otherwise specified, all chemicals were procured from Merck (Germany).

2.2. Synthesis of the Fe_3O_4@SB nanocomposite

To synthesize the Fe_3O_4@SB nanocomposite, 1.4 g (8 mmol) of benzene-1,4-dicarboxaldehyde (BDC) was dissolved in 70 mL of toluene. This solution was added to the 3-aminopropyltrimethoxysilane (APTMS)-modified magnetite nanoparticles. The mixture was heated under reflux at 100 °C for 48 h under a nitrogen atmosphere. After the reaction was complete, the product was washed three times with toluene and separated from the solution using a permanent magnet. The final nanocomposite was dried at 60 °C for 12 h. The overall synthesis route is illustrated in Scheme 1.

Scheme 1. The synthesis procedure of Fe_3O_4@SB nanocomposite.

2.2.1. Synthesis of magnetite nanoparticles (Fe_3O_4 NPs)

The alkaline co-precipitation technique, which utilizes ferrous (Fe^{2+}) and ferric (Fe^{3+}) chloride salts as precursors, was employed to synthesize magnetite nanoparticles (Fe_3O_4). This well-established method was selected because it is operationally straightforward, cost-effective, and scalable, producing nanoparticles with high magnetic susceptibility and a controlled size distribution, properties essential for subsequent surface functionalization processes [20, 21].

A homogeneous solution was prepared by dissolving $FeCl_2.4H_2O$ (3.17 g, 0.016 mol) and $FeCl_3.6H_2O$ (7.56 g, 0.028 mol) in 100 mL of distilled water, corresponding to a Fe^{2+}: Fe^{3+} molar ratio of approximately 1:2. The mixture was then heated to 60°C while being continuously purged with nitrogen (N_2) to prevent the oxidation of Fe^{2+} to Fe^{3+}. This step is crucial to ensure the formation of stoichiometric magnetite with phase purity and to inhibit the synthesis of maghemite (γ-Fe_2O_3) [22]. Maintaining an inert atmosphere during this stage is essential. Precipitation was initiated by the gradual addition of 11 mL of a 25% aqueous ammonia solution, raising the pH to approximately 10. The rapid formation of a black precipitate indicated successful nucleation and growth of magnetite nanoparticles. The resulting suspension was stirred continuously for an additional 30 minutes to promote complete particle formation.

A permanent magnet was used to separate the synthesized Fe_3O_4 nanoparticles (Fe_3O_4 NPs) from the reaction mixture. The recovered magnetic solid was repeatedly washed with ethanol and distilled water until the supernatant reached a neutral pH, ensuring the removal of ionic contaminants and reaction byproducts. To obtain a stable powder, the purified nanoparticles were dried in an oven at 70°C for 24 h.

2.2.2. Surface functionalization with APTMS (Fe_3O_4@NH_2)

3 g of the synthesized magnetite nanoparticles were dispersed in 150 mL of a 1:1 (v/v) water-ethanol solution. The mixture was then heated under reflux. Subsequently, 3 mL of 3-aminopropyltrimethoxysilane (APTMS) was added, and the reaction was continued under a nitrogen atmosphere at reflux temperature for 2 h. After the reaction, the modified nanoparticles were collected magnetically by placing a permanent magnet beneath the beaker and decanting the supernatant. The product was washed twice with distilled water and ethanol, then dried at room temperature.

2.3. Characterization techniques

Analyses were performed on a Bruker Tensor 27 spectrometer (Bruker, Germany) to identify functional groups and confirm the success of chemical bonding and functionalization steps. Crystallographic structure and phase purity were determined using a Philips X'Pert diffractometer (Malvern Panalytical, UK) with Cu Kα radiation (λ

= 1.54 Å). Data were collected over a 2θ range of 5° to 80°. The magnetic properties were investigated at room temperature using a VSM system (Maghnatis Danesh-pajooh Kashan Co., Iran), with applied fields of up to 15 kOe, to assess saturation magnetization and superparamagnetic behavior. Textural properties, including specific surface area, pore volume, and pore size distribution, were derived from nitrogen adsorption-desorption isotherms measured at 77 K using a NOVA win2m analyzer (Quantachrome, USA). The surface morphology and topography of the nanomaterials were examined using a VEGA/TESCAN-LMU microscope (TESCAN, Czech Republic). Qualitative elemental analysis was performed using an EDX detector coupled to the SEM. The residual concentrations of the target pharmaceutical compounds in solution were quantified using a Shimadzu UV-1650PC spectrophotometer (Japan).

2.4. Determination of the point of zero charge (pHpzc)

The point of zero charge (pHpzc) of the Fe_3O_4@SB nanocomposite was determined using the solid addition method [23]. A series of 50 mL solutions of 0.01 M NaCl was prepared in sealed conical flasks. The initial pH (pH_i) of each solution was adjusted to values between 2 and 10 using 0.1 M HCl or NaOH. Then, 0.05 g of the Fe_3O_4@SB adsorbent was added to each flask. The suspensions were agitated for 24 hours at room temperature (25 ± 1 °C) to reach equilibrium. Subsequently, the solid was separated magnetically, and the final pH (pH_f) of the supernatant was measured. The difference $\Delta pH = pH_f - pH_i$ was calculated and plotted against the initial pH_i. The pHpzc is identified as the point where the curve $\Delta pH = 0$ intersects the pH_i axis, indicating the pH at which the net surface charge of the adsorbent is zero.

2.5. Adsorption experiments

To ensure the measured removal was solely due to adsorption on Fe_3O_4@SB, control experiments were conducted with PhAC solutions at each optimal pH in the absence of adsorbent. No significant decrease in concentration was observed, ruling out substantial adsorption performance or precipitation under the experimental conditions. All reported removal efficiencies are therefore attributable to adsorption onto the nanocomposite.

The adsorption efficacy of the synthesized Fe_3O_4@SB nanocomposite was evaluated for the removal of MA, TRP, and 5-FU. Batch adsorption experiments were conducted by adding 5 mg of Fe_3O_4@SB to separate 100 mL beakers, each containing 10 mL of a target pharmaceutical solution at an initial concentration of 5 mg L^{-1}. The solution pH was adjusted to its optimized value (pH 4 for MA, pH 6 for TRP, and pH 8 for 5-FU) using dilute NaOH or HCl. The mixtures were agitated for 10 min using a magnetic stirrer. The magnetic Nano adsorbent was then separated using an external magnet, and the residual concentration of the pharmaceutical in the supernatant was quantified by UV/Vis spectrophotometry at λ_{max} = 288 nm (MA), 280 nm (TRP), and 266 nm (5-FU). Analyte concentrations were determined using pre-constructed external calibration

curves. A control experiment with the Nano adsorbent in distilled water at pH 4 confirmed no contribution from the adsorbent to the absorbance. All experiments were performed in triplicate.

2.6. Preparation of calibration standard solutions

A series of standard solutions was prepared, and corresponding calibration curves were constructed to enable quantitative analysis of the target pharmaceutical compounds throughout the adsorption experiments.

For MA, a stock solution of 100 mg L^{-1} was initially prepared. Subsequent dilutions yielded working standards, including a 10 mg L^{-1} solution prepared by diluting 2.5 mL of stock to 25 mL with distilled water. The UV-Vis absorption spectrum of this solution was recorded against a distilled water blank across the 200–400 nm range, confirming λ_{max} at 288 nm. Similarly, working standards of TRP at 10 mg L^{-1} and 5-FU at 5 mg L^{-1} were prepared, with their respective λ_{max} values confirmed at 280 nm and 266 nm.

For quantitative determination, individual calibration curves were established for each compound under its optimal pH conditions. For MA, seven standard solutions (2–25 mg L^{-1}) were prepared at pH 4, and absorbance was measured at 288 nm. For TRP, standards ranging from 2–50 mg L^{-1} were prepared at pH 6, with measurements at 280 nm. For 5-FU, standards from 2–10 mg L^{-1} were prepared at pH 8, with measurements at 266 nm. In all cases, absorbance values were measured against pH-adjusted blanks, and linear regression was performed to establish the relationship between absorbance and concentration, providing the calibration model for subsequent quantification in adsorption studies.

2.7. Study of factors influencing removal

2.7.1. Effect of pH

The influence of solution pH on adsorption efficiency was evaluated by preparing a series of solutions (10 mL, 5 mg L^{-1}) for each pharmaceutical at different pH values (2–10). A fixed mass of 5 mg of Fe_3O_4@SB was added to each beaker. The mixtures were agitated for 5 min, after which the adsorbent was magnetically separated. The residual concentration was determined spectrophotometrically, and the removal percentage was calculated for each pH to identify the optimum condition.

2.7.2. Effect of contact time

Adsorption kinetics were evaluated by agitating mixtures of pharmaceutical solution (10 mL, 5 mg L^{-1} at optimal pH) and 5 mg of Fe_3O_4@SB for varying time intervals (1, 2, 5, 10, 15, 20, and 30 min). After each interval, the adsorbent was separated, and the residual concentration was measured to calculate the removal percentage over time.

2.7.3. Effect of adsorbent dosage

The effect of adsorbent mass was investigated by adding varying amounts of Fe_3O_4@SB (1, 2, 4, 5, 7, and 10 mg) to pharmaceutical solutions (10 mL, 5 mg L^{-1} at optimal pH). The mixtures were agitated for 5 min, and the residual concentration was measured after magnetic separation to determine the optimal dosage.

2.8. Investigation of adsorption isotherms

Adsorption isotherm studies were conducted to elucidate the equilibrium distribution of adsorbate molecules between the aqueous phase and the solid adsorbent surface. These experiments provide critical insight into the adsorption capacity and the nature of the interactions between the pharmaceutical compounds and the Fe_3O_4@SB nanocomposite. The adsorption isotherm for MA was constructed using a series of experiments with 20 mL aliquots of MA solution at varying initial concentrations (30-600 mg L^{-1}), adjusted to the optimal pH of 4. A fixed mass of 5 mg of Fe_3O_4@SB was introduced to each solution, and the mixtures were agitated for 1 h to ensure adsorption equilibrium. Following magnetic separation of the adsorbent, the equilibrium concentration (C_e) of MA in the supernatant was determined spectrophotometrically at λ_{max} = 288 nm.

The equilibrium adsorption capacity, Q_e (mg g^{-1}), was calculated for each initial concentration using the following mass balance equation (1):

$$\mathbf{Q_e = (C_o - C_e)\ V/m} \qquad (1)$$

Where C_o represents the initial concentration (mg L^{-1}), C_e the equilibrium concentration (mg L^{-1}), V the solution volume (L), and m the adsorbent mass (g).

This methodology was similarly applied to investigate the adsorption isotherms for TRP (pH 6) and 5-FU (pH 8). The resulting equilibrium data (Q_e versus C_e) were fitted to both Langmuir and Freundlich isotherm models to analyze the adsorption mechanism and quantify the maximum adsorption capacity.

3. Results and discussion

3.1. Structural characterizations

3.1.1. FT-IR spectroscopy analysis

Fig. 1a shows the FT-IR spectrum of the synthesized magnetite nanoparticles (Fe_3O_4 NPs). The characteristic peaks corresponding to the Fe–O bond in magnetite are observed at 565 cm^{-1} and 425 cm^{-1}. The broad peak at 3415 cm^{-1} and the sharper peak at 1620 cm^{-1} are attributed to the stretching and bending vibrations, respectively, of surface-adsorbed water molecules and hydroxyl groups [21, 24].

Fig. 1b displays the FT-IR spectrum of the Fe_3O_4@NH_2 nanoparticles. To graft amino groups onto the magnetite surface, 3-aminopropyltrimethoxysilane (APTMS) was used. In this reaction, the methoxy groups are hydrolyzed, forming Si–O–Si bonds that anchor the aminopropyl groups to the nanoparticle surface via Fe–O–Si linkages. In addition to the Fe–O peak at 576 cm^{-1}, a new absorption band at 995 cm^{-1} confirms the presence of

Fe–O–Si bonds. The broad peak at 3500 cm^{-1} and the sharper peak at 1602 cm^{-1} correspond to the stretching and bending vibrations of N–H bonds and residual water hydroxyl groups, respectively [25].

Fig. 1c presents the FT-IR spectrum of the final Fe_3O_4@SB nanocomposite. The successful formation of the Schiff base network is confirmed by the peak at 1691 cm^{-1}, which is characteristic of the imine (C=N) bond formed between the aldehyde groups of benzene-1,4-dicarboxaldehyde (BDC) and the primary amine groups of the APTMS modifier. Furthermore, the appearance of new peaks at 1778 cm^{-1} (C=O), 1203 cm^{-1} (C–O), and 1358 cm^{-1} (C–C) corroborates the formation of an organic layer on the nanoparticle surface via the Schiff base reaction.

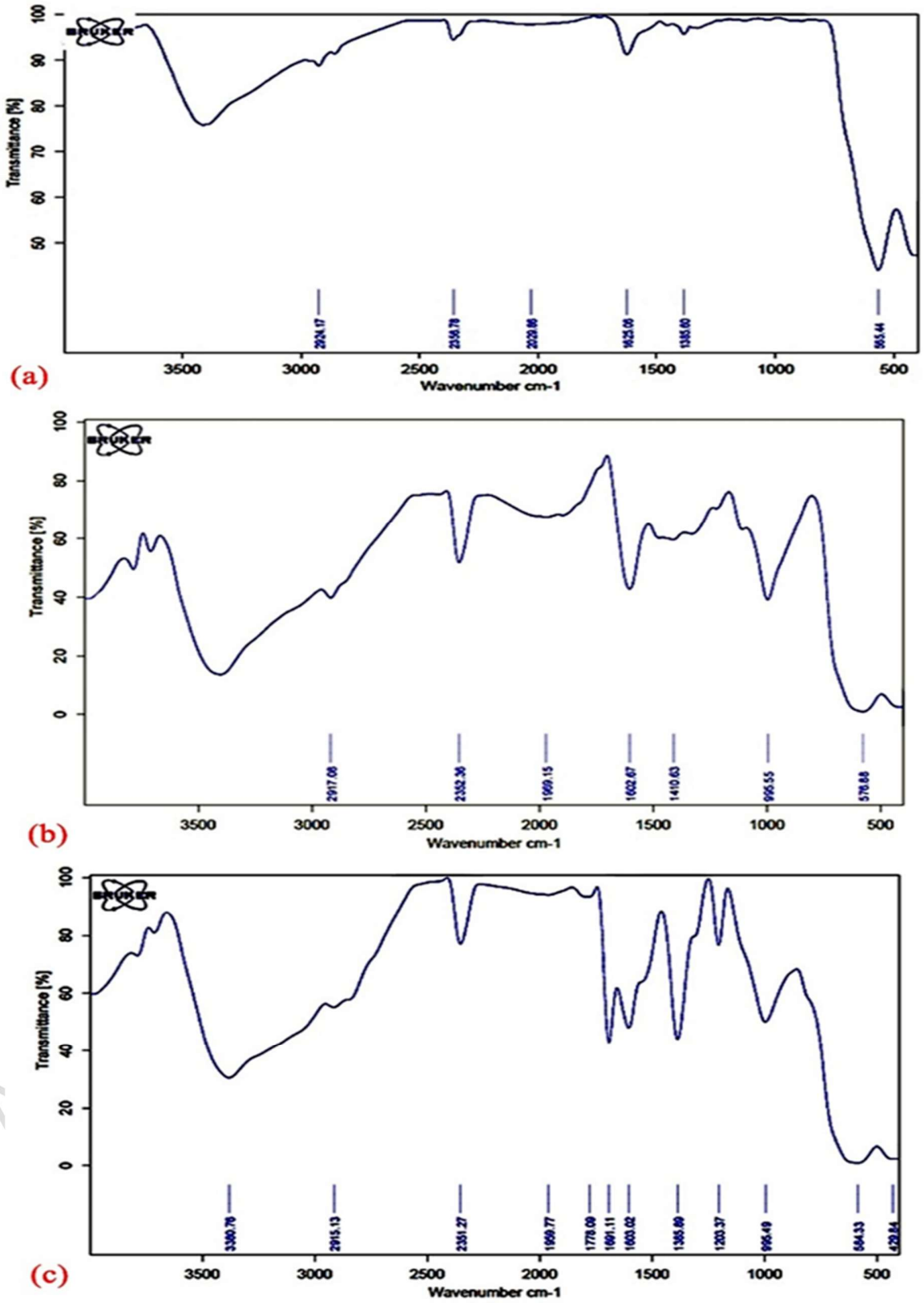

Figure 1. FT-IR spectrum of (a) Fe_3O_4 NPs, (b) Fe_3O_4-APTMS, (c) Fe_3O_4@SB

3.1.2. X-ray diffraction

Figs. 2a-c present the XRD patterns of the Fe_3O_4 NPs, Fe_3O_4@NH_2, and Fe_3O_4@SB, respectively. All observed diffraction peaks in these patterns could be indexed to the cubic spinel structure of magnetite (JCPDS card No. 01-075-0449) [26, 27]. The characteristic peaks at 2θ values of approximately 30.1°, 35.5°, 43.1°, 53.5°, 57.0°, and 62.6° correspond to the (220), (311), (400), (422), (511), and (440) crystallographic planes, respectively. This confirms the successful synthesis of crystalline Fe_3O_4 NPs. The most intense peak, corresponding to the (311) plane, was used for crystallite size calculation. Table 1 reports the primary diffraction peaks and the corresponding Miller indices (hkl). The absence of characteristic peaks for goethite (α-FeOOH) at 2θ = 21.2° (110) and hematite (α-Fe_2O_3) at 33.15° (104) indicates the high phase purity of the synthesized magnetite, free from common oxidative by-products. Maghemite (γ-Fe_2O_3), a fully oxidized form with a similar spinel structure, typically shows a nearly identical pattern to magnetite but may exhibit peak broadening or weak super-lattice reflections [22, 28]. The absence of such features, combined with the controlled synthesis under a nitrogen atmosphere to prevent Fe^{2+} oxidation, strongly supports the formation of stoichiometric Fe_3O_4. Furthermore, no diffraction peaks corresponding to hematite (α-Fe_2O_3), such as its most intense (104) reflection at 33.15° (JCPDS 33-0664), were detected, confirming the absence of this thermodynamically stable oxidative end-product [27]. Most importantly, the consistency in the position and profile of the magnetite diffraction peaks across the pristine (Fe_3O_4 NPs), salinized (Fe_3O_4@NH_2), and polymer-grafted (Fe_3O_4@SB) samples demonstrates that the core crystal structure of magnetite remains intact and stable throughout the sequential surface functionalization processes [30]. This confirms that the chemical modifications are confined to the nanoparticle surface without inducing a phase transformation in the magnetic core.

The well-known Scherrer equations (2) and (3) were used to calculate the average crystallite size using the full width at half maximum (FWHM) of the most intense (311) peak [29]:

$$D = \frac{k.\lambda}{\beta.\cos\theta} \quad (2)$$

$$\beta = \frac{FWHM \times \pi}{180} \quad (3)$$

The Bragg angle is θ, the complete width at half maximum (FWHM) of the diffraction peak is β, the X-ray wavelength is λ (0.15 nm), the shape factor is K (0.9), and the crystallite size is D. The calculated average crystallite sizes were 9.4 nm for the pristine Fe_3O_4 NPs, 10.6 nm for Fe_3O_4@NH_2, and 21.2 nm for Fe_3O_4@SB. The consistency of the peak positions across the pristine and functionalized samples (Fe_3O_4 NPs, Fe_3O_4@NH_2,

Fe_3O_4@SB) confirms that the surface modifications with APTMS and the subsequent Schiff base network growth did not alter the core magnetite crystal structure **[30]**.

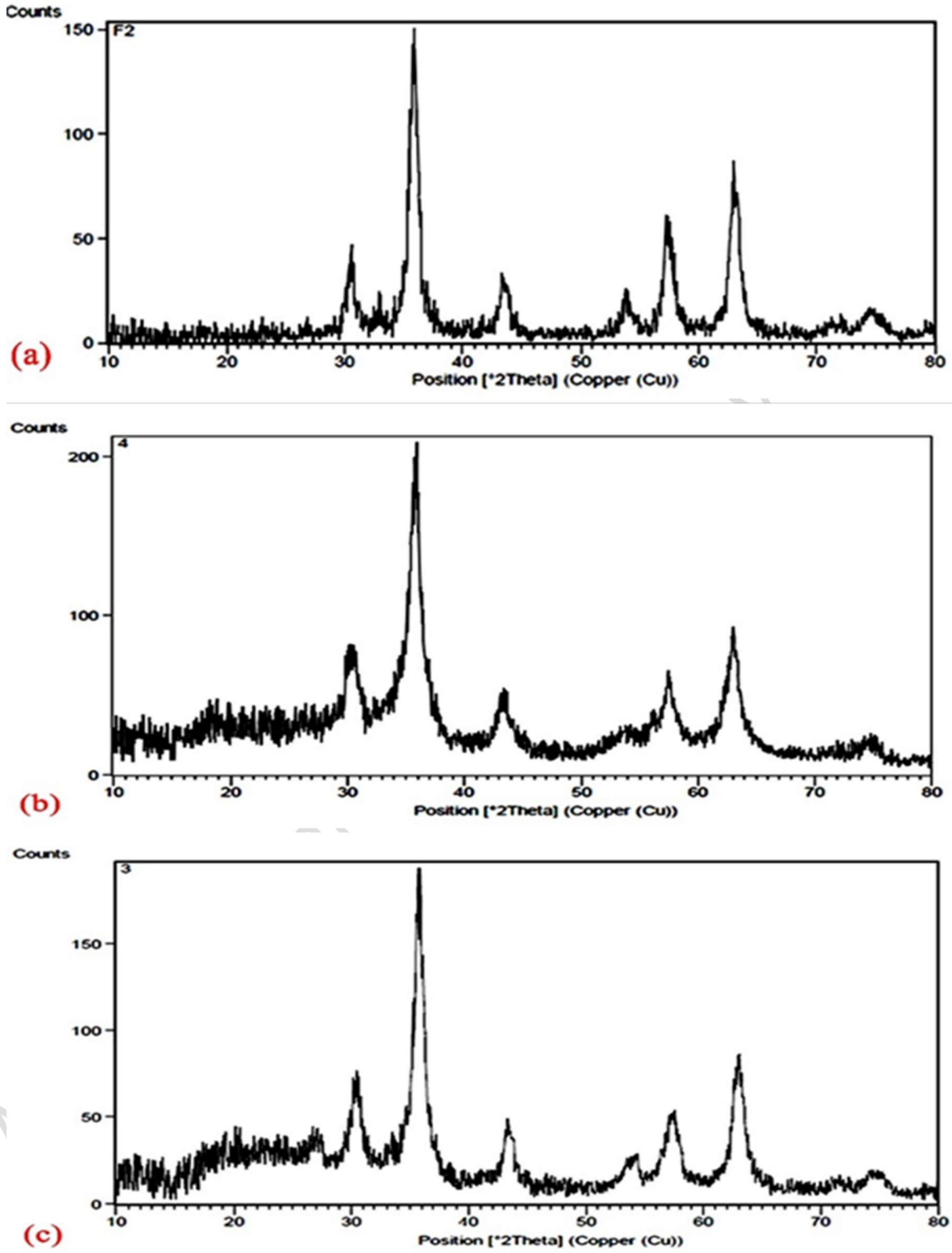

Figure 2. XRD pattern of (a) Fe_3O_4 NPs, (b) Fe_3O_4@NH_2, and (c) Fe_3O_4@SB

Table 1. The primary diffraction peaks and the corresponding Miller indices

2θ (approx., Cu Kα)	Miller Indices (hkl)	Relative Intensity
~18.3°	(111)	Low
~30.1°	(220)	Medium
~35.5°	(311)	Very High
~37.1°	(222)	Low
~43.1°	(400)	Medium
~53.5°	(422)	Medium
~57.0°	(511)	Medium
~62.6°	(440)	High

3.1.3. VSM analysis

Figs. 3a-c and Table 2 show the magnetic field-dependent magnetization parameters M(H) for Fe_3O_4 NPs, Fe_3O_4@NH_2, and Fe_3O_4@SB at room temperature using a vibrating sample magnetometer in a field of 15 kOe. The presence of superparamagnetic behavior in Fe_3O_4 is confirmed by the absence of a hysteresis loop in the magnetization curve of this compound, which is a characteristic feature of single-domain magnetic nanoparticles at room temperature [26]. The saturation magnetization of the pristine Fe_3O_4 NPs was found to be 60 emu g^{-1} with negligible coercivity (H_c = 0.0 Oe) and remanence (M_r = 0.0 emu g^{-1}), demonstrating excellent superparamagnetic properties crucial for magnetic separation applications [8].

After sequential functionalization, the VSM curves of both Fe_3O_4@NH_2 and Fe_3O_4@SB nanocomposites retained their superparamagnetic nature, as evidenced by the lack of hysteresis. However, the saturation magnetization values decreased to 42 emu g^{-1} and 30 emu g^{-1}, respectively. This reduction is a well-documented phenomenon and can be attributed to the increased mass of the non-magnetic organic coating (the Schiff base network) surrounding the magnetic core, which effectively dilutes the magnetic moment per unit mass [7]. Furthermore, the surface functionalization layers can introduce spin-canting or disrupt the magnetic coupling between neighboring Fe_3O_4 NPs, leading to a lower observed M_s [21]. Despite this reduction, the Fe_3O_4@SB nanocomposite retains a sufficiently high M_s of 30 emu g^{-1}, ensuring rapid and facile separation from aqueous solution using an external magnet, a key advantage for adsorbent recyclability.

Table 2. The Magnetic properties of Fe_3O_4 NPs, Fe_3O_4@NH_2 and Fe_3O_4@SB

Samples	M_s (emu g^{-1})	H_c (Oe)	M_r (emu g^{-1})
Fe_3O_4	60	0	0
Fe_3O_4@NH_2	42	0	0
Fe_3O_4@SB	30	0	0

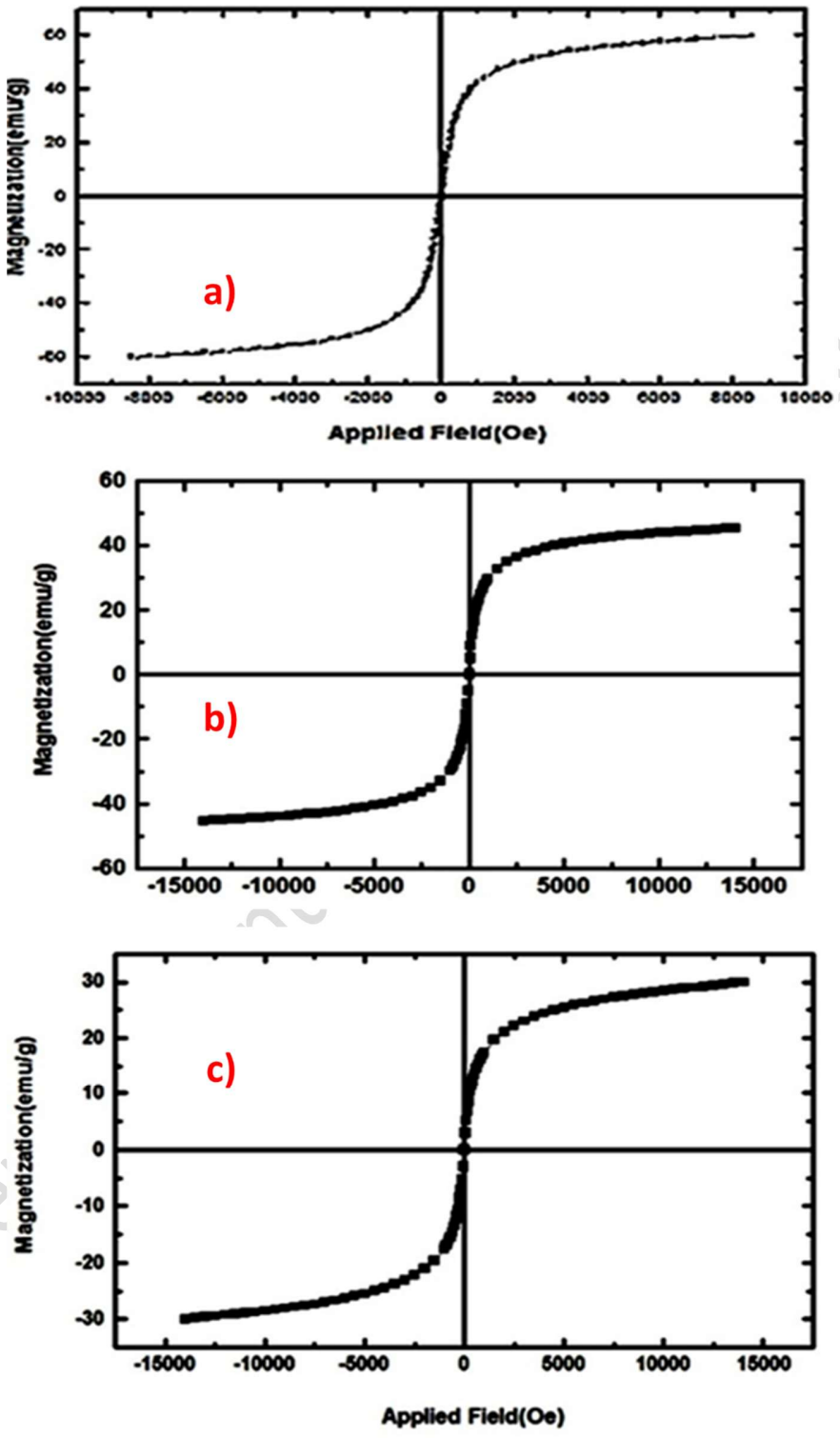

Figure 3. VSM analysis graph of (a) Fe_3O_4 NPs, (b) Fe_3O_4@NH_2, and (c) Fe_3O_4@SB

3.1.4. SEM images

Figs. 4a-c shows the scanning electron microscopy (SEM) images of the Fe_3O_4 NPs, Fe_3O_4@NH_2 and Fe_3O_4@SB nanocomposite at high magnifications. The images in Fig. 4a demonstrate a good homogeneous distribution of spherical nanoparticles, which is a characteristic morphology for magnetite nanoparticles synthesized via the co-precipitation method [21].

After surface modification with APTMS (see Fig. 4b), the overall spherical shape of the nanoparticles was preserved, indicating that the salinization process did not alter the core morphology. However, a closer comparison reveals that the Fe_3O_4@NH_2 NPs appear slightly less defined and show minimal signs of aggregation, which is a common outcome of successful surface functionalization that introduces organic layers and reduces inter-particle magnetic dipole interactions [8].

Critically, in the image of the final Fe_3O_4@SB nanocomposite (see Fig. 4c), the nanoparticles exhibit a distinctly rough surface topography and a more aggregated, cluster-like morphology. This visible alteration is a strong indicator of the successful formation of a Schiff base deposition layer on the surface of the nanoparticles. The growth of covalent organic frameworks or porous polymer networks on magnetic cores often results in such surface roughening and an increase in particle size, as the organic matrix encapsulates the individual nanoparticles [16, 18]. This observed morphological evolution from smooth spheres to a coarse texture provides clear visual evidence for the successful construction of the mesoporous Fe_3O_4@SB nanocomposite.

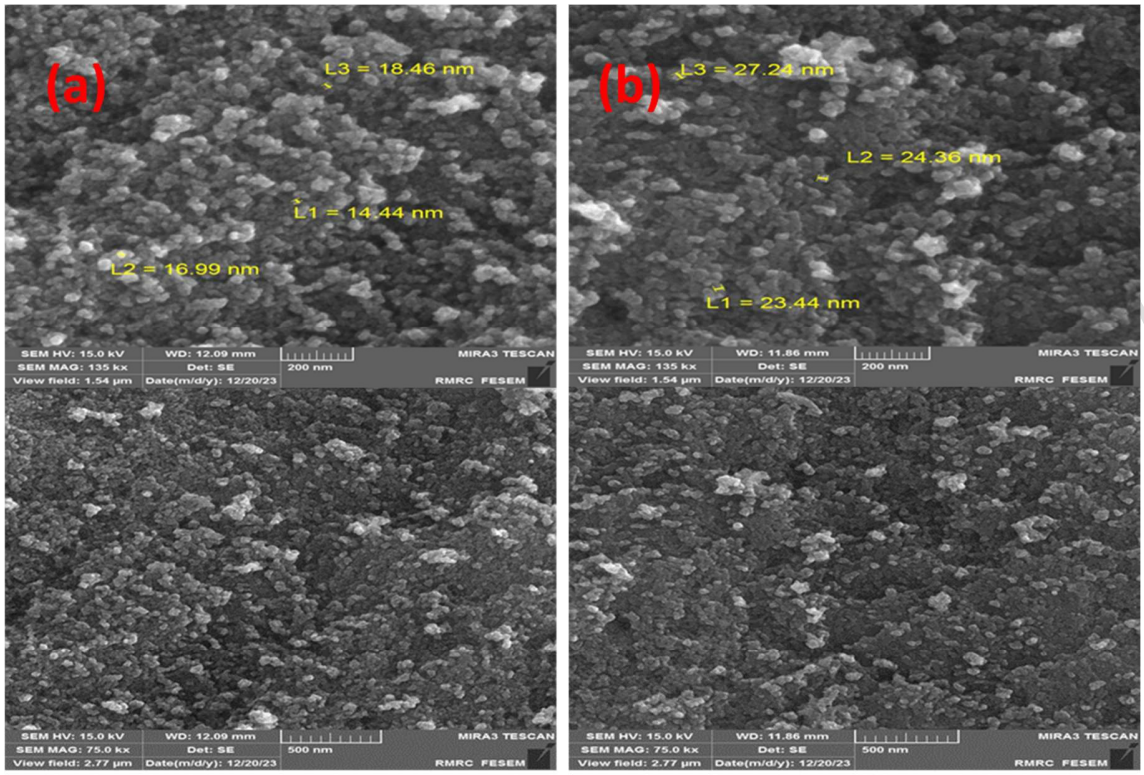
(a)
L3 = 18.46 nm
L1 = 14.44 nm
L2 = 16.99 nm
(b)
L3 = 27.24 nm
L2 = 24.36 nm
L1 = 23.44 nm

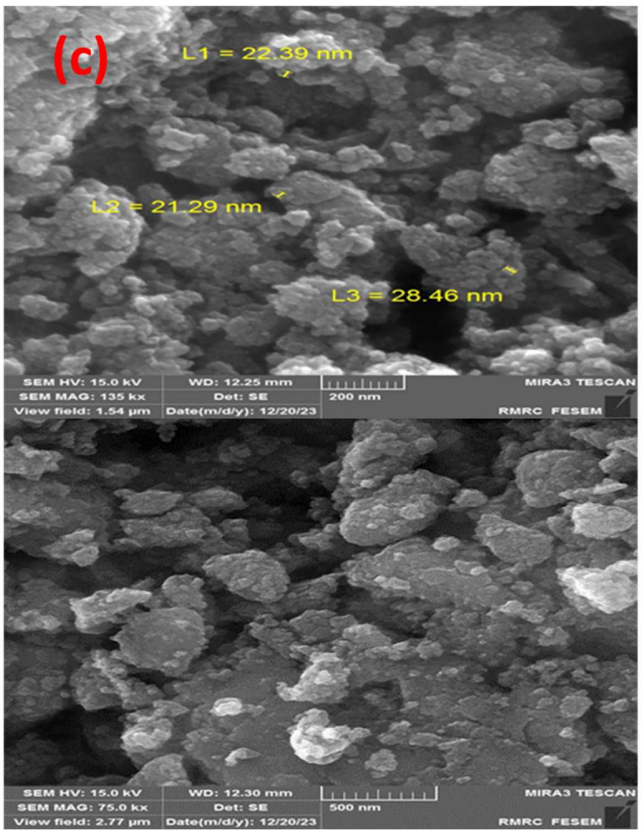
(c)
L1 = 22.39 nm
L2 = 21.29 nm
L3 = 28.46 nm

Figure 4. SEM images of (a) Fe_3O_4 NPs, (b) Fe_3O_4@NH_2, and (c) Fe_3O_4@SB

3.1.5. EDAX analysis

Figs. 5a-b show the energy dispersive X-ray analysis (EDAX) data. The EDAX spectrum in Fig. 5a confirms the presence of Fe and O as the primary elements in the magnetite nanoparticles, which is consistent with the expected composition of pure Fe_3O_4 and aligns with findings from other studies [31, 32]. The subsequent appearance of a silicon (Si) signal in the EDAX spectrum of Fe_3O_4@NH_2 (see Fig. 5b) provides direct evidence for the successful grafting of the amino silane (APTMS) coupling agent onto the nanoparticle surface. Most critically, the EDAX spectrum of the final Fe_3O_4@SB nanocomposite (see Fig. 5c) reveals distinct peaks for carbon (C) and nitrogen (N), in addition to Fe, O, and Si. This elemental profile conclusively confirms the successful formation of the Schiff base organic network on the nanoparticle surface, a finding supported by similar EDX data in other functionalized magnetic nanocomposites [33].

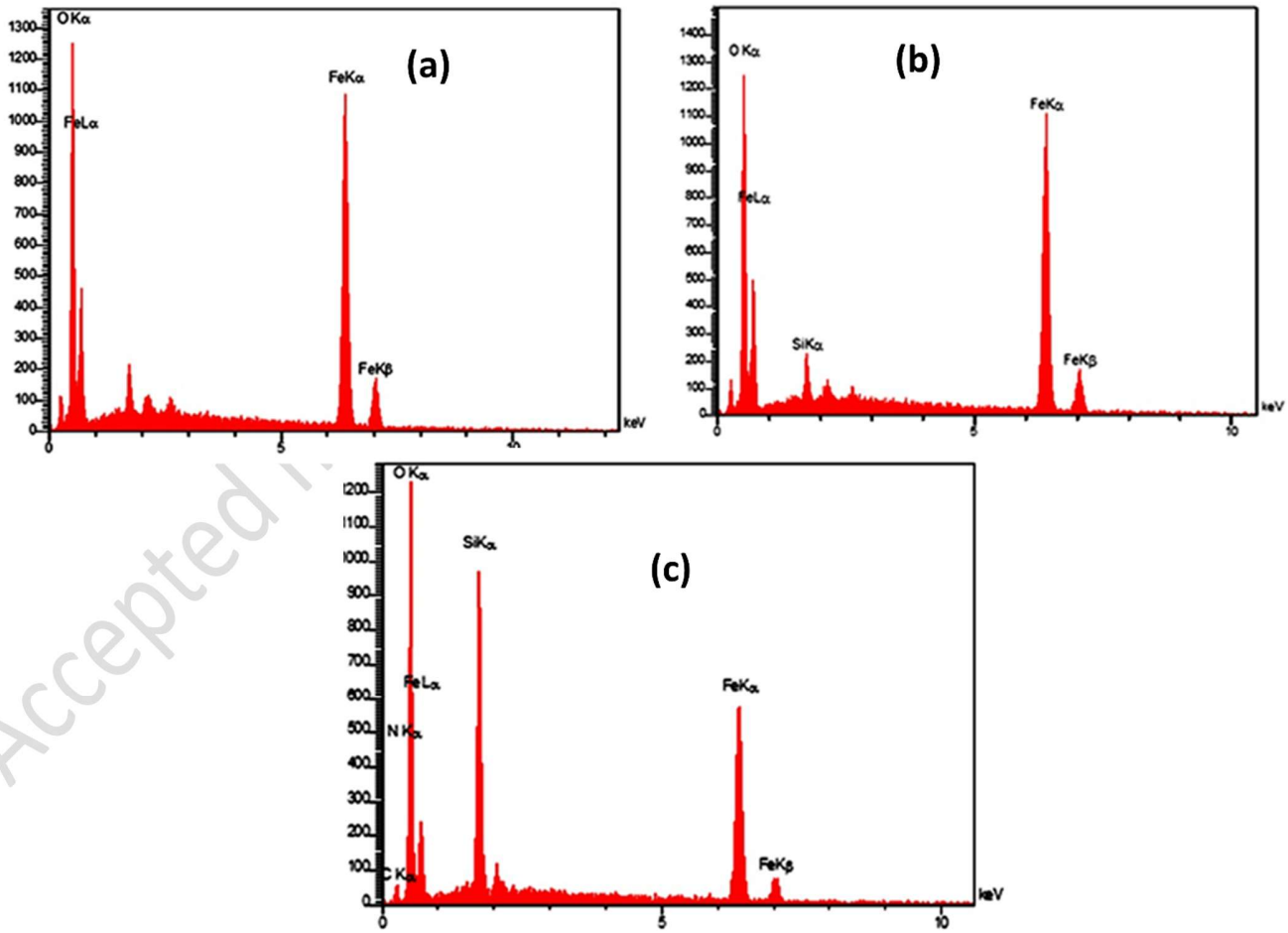

Figure 5. EDAX analysis of (a) Fe_3O_4 NPs, (b) Fe_3O_4@NH_2, and (c) Fe_3O_4@SB

3.1.6. BET and BJH analysis

The textural properties of the Fe_3O_4@SB nanocomposite were investigated using N_2 adsorption-desorption measurements at 77 K (see Fig. 6a). The Barrett-Joyner-Halenda (BJH) model, a standard method for evaluating the pore size distribution of mesoporous materials [34], was applied to the desorption branch of the isotherm. The Brunauer-Emmett-Teller (BET) model revealed a specific surface area of 17.687 $m^2\ g^{-1}$. Although the BET surface area is moderate compared to some high-surface-area adsorbents, the presence of functional Schiff base groups and magnetic Fe_3O_4 cores significantly enhances adsorption efficiency. Comparable or even superior performance has been reported for functionalized materials with similar surface areas [16, 35]. The importance of textural properties like surface area and porosity in determining the efficacy of Fe_3O_4-based nanomaterials for environmental remediation has been widely highlighted [7]. The total pore volume was 4.467 $cm^3\ g^{-1}$, confirming a highly porous structure. The BJH model yielded an average pore diameter of 10.554 nm, which classifies the material as mesoporous (see Fig. 6b). This pore size is consistent with studies on other carbon-encapsulated magnetite systems [35] and is highly favorable for accommodating the target pharmaceutical molecules. The average pore diameter (~10.55 nm) is significantly larger than the molecular dimensions of tryptophan, mefenamic acid, and 5-fluorouracil, facilitating molecular diffusion and adsorption. Although computational modelling was not performed, experimental adsorption results confirm effective accommodation of all three PhACs within the mesoporous structure.

The Langmuir surface area was calculated to be 19.83 $m^2\ g^{-1}$ (see Fig. 6c). The high C value of 24.381 derived from the BET equation (see Fig. 6d) indicates a strong interaction energy between the adsorbent surface and the first layer of nitrogen molecules, reflecting a high adsorption affinity.

In summary, the Fe_3O_4@SB nanocomposite possesses a significant surface area, a well-defined mesoporous network, and a strong affinity for adsorbates. These textural characteristics are highly favorable for applications in adsorption, catalysis, and storage. A summary of these parameters is provided in Table S1 (Supplementary Information).

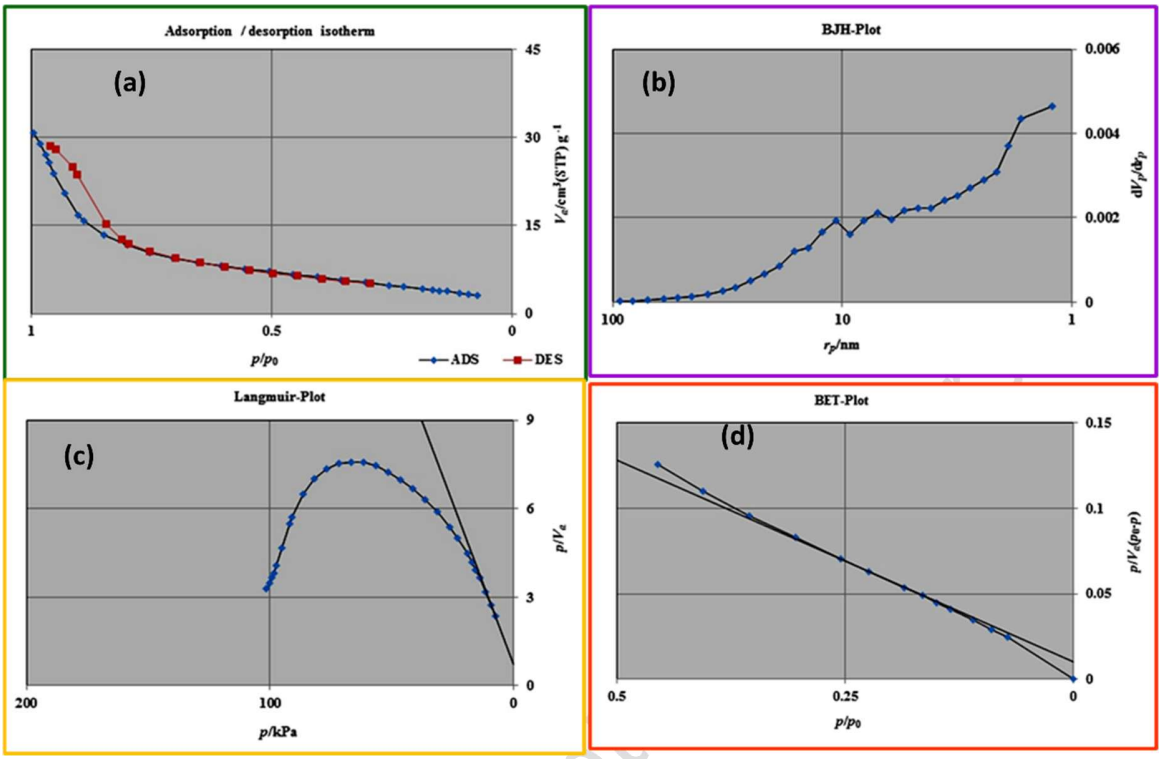

Figure 6. (a) Nitrogen adsorption/desorption isotherm for Fe_3O_4@SB, (b) BJH plot, (c) Langmuir plot, and (d) BET plot

3.1.7. Point of Zero Charge (pHpzc)

The pHpzc of the Fe_3O_4@SB nanocomposite was determined to be approximately 6.2. This value is critical for interpreting the pH-dependent adsorption behavior. At pH < pHpzc, the adsorbent surface is positively charged due to protonation of amine/imine groups. At pH < pHpzc, the surface is positively charged (protonation of amine/imine groups dominates), while at pH > pHpzc, the surface becomes negatively charged due to deprotonation. This parameter directly influences electrostatic interactions with ionizable pharmaceutical compounds.

3.2. UV-Vis spectrophotometric analysis

The quantitative analysis of the target pharmaceutical compounds was performed using UV-Vis spectrophotometry, a well-established technique prized for its sensitivity, simplicity, and reliability in determining analyte concentrations [36, 37]. The absorption spectra for MA, TRP, and 5-FU were recorded (see Figs. 7a-c), showing distinct λ_{max} at 288 nm, 280 nm, and 266 nm, respectively. The corresponding spectral data are detailed in Tables S2-S4 (Supplementary Information).

Linear calibration curves were established for each compound at its optimal pH, following a standard practice in quantitative spectrophotometric analysis (see Figs. 8a-c) [36]. The excellent linearity of all calibration curves, with correlation coefficients (R^2) greater than 0.99, provides a robust foundation for accurate quantification and is consistent with the performance of UV-Vis methods reported in other recent studies, including those involving magnetic nanocomposites [38] and pharmaceutical analysis [39].

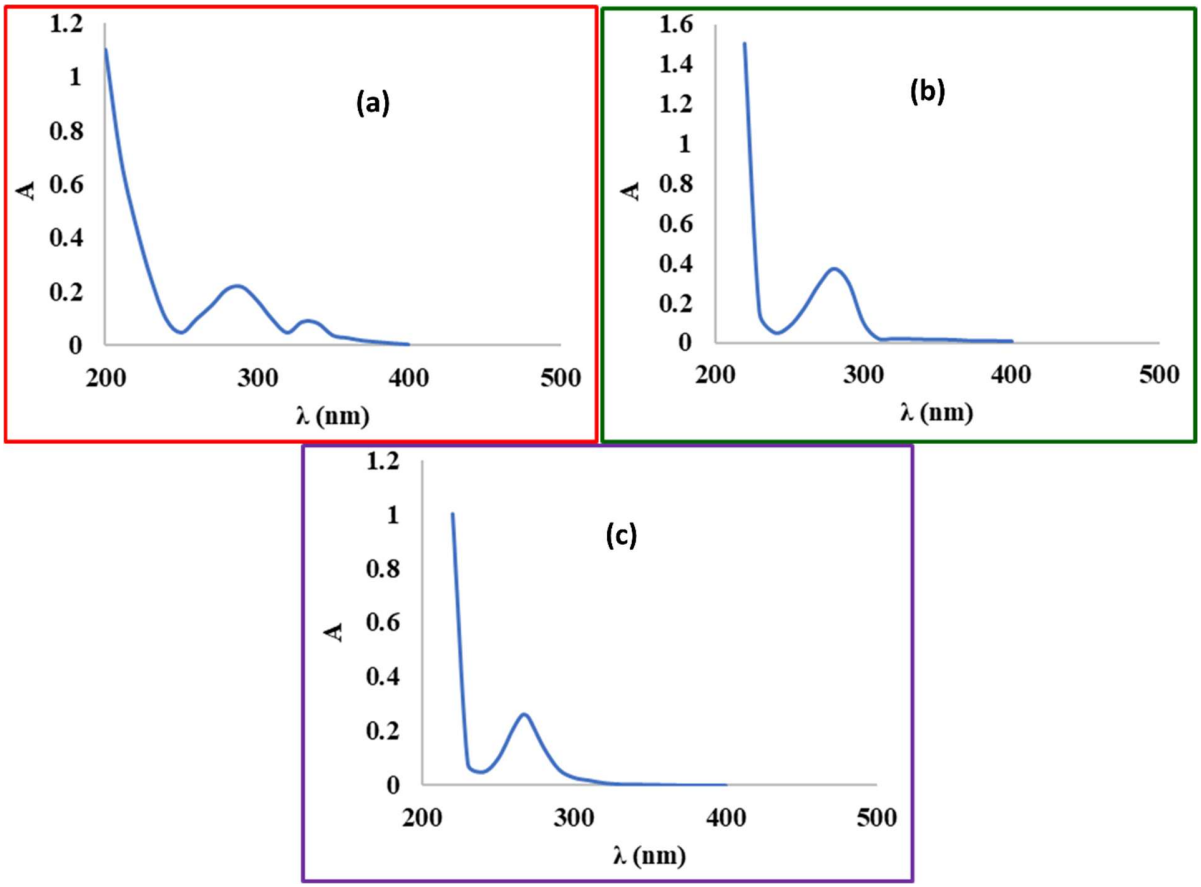

Figure 7. UV/Vis absorption spectra of (a) MA, (b) TRP, and (c) 5-FU

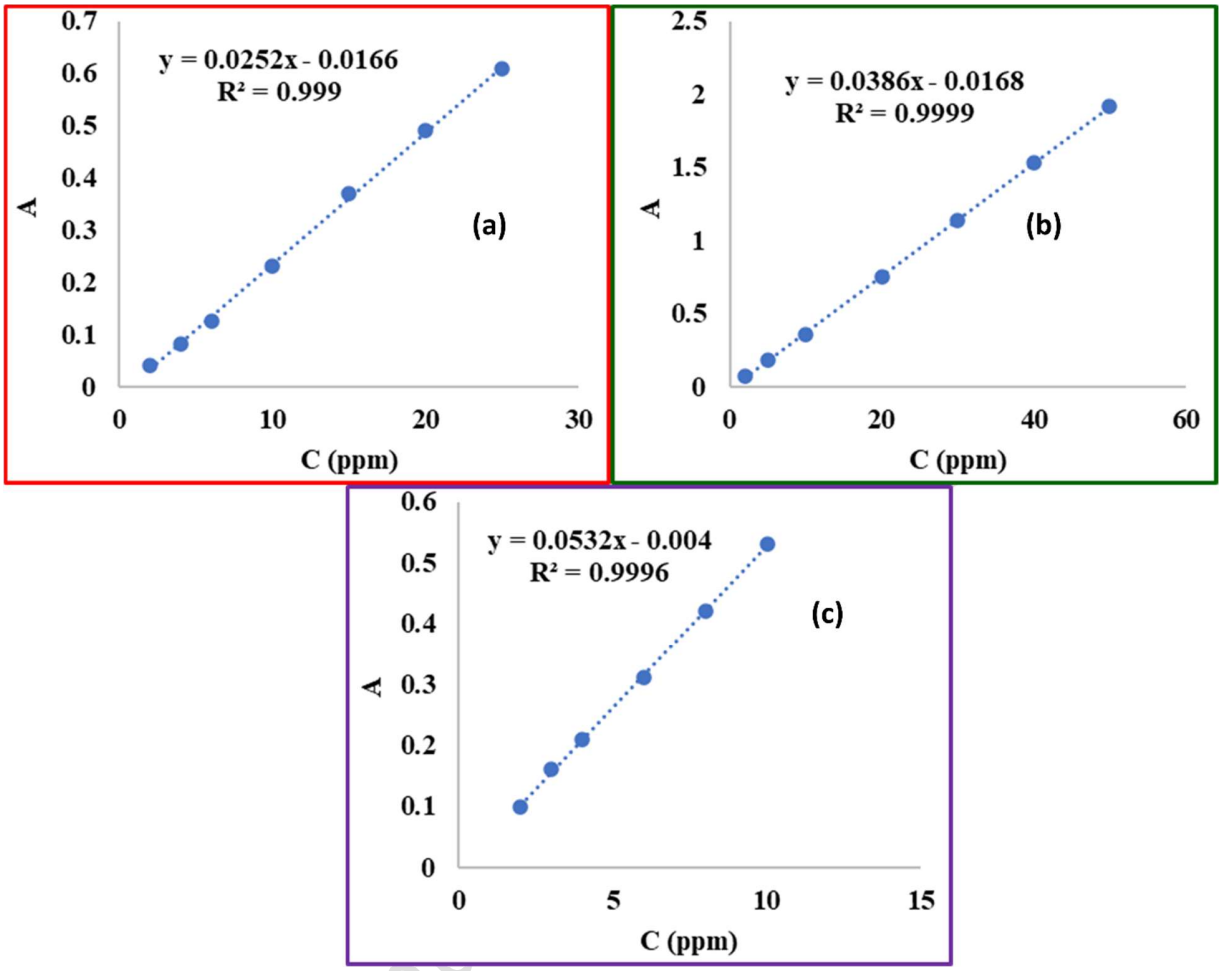

Figure 8. Calibration curves for (a) MA, (b) TRP, and (c) 5-FU

3.3. Evaluation of PhACs removal

The adsorption performance of the Fe_3O_4@SB nanocomposite was quantitatively assessed. The removal efficiency (%R) was calculated using the following mass balance equation (4):

$$\%R = (C_o - C_e) / C_o \times 100 \quad (4)$$

Where C_o and C_e are the initial and equilibrium concentrations (mg L^{-1}), respectively. Under their respective optimized conditions, the Fe_3O_4@SB nanocomposite demonstrated exceptional removal efficiencies, achieving 98.07% for MA, 98.27% for TRP, and 96.53% for 5-FU, as summarized in Table 3. These results, exceeding 96% for all three target PhACs, position the nanocomposite as a highly competitive adsorbent [40, 41]. The identified optimal pH values, pH 4 for MA, pH 6 for TRP, and pH 8 for 5-FU, are

consistent with the typical optimal range reported for the adsorption of weakly acidic pharmaceuticals onto engineered adsorbents [42].

The precision and reliability of the adsorption process were confirmed through repeatability studies. The low relative standard deviation (RSD) values for both intra-day (1.27–2.18%) and inter-day (1.23–2.02%) experiments, as presented in Table 4, demonstrate that the Fe_3O_4@SB nanocomposite exhibits highly consistent and stable adsorption performance. Slight variations in environmental conditions may explain the marginally higher intraday RSD. Overall, the consistently low RSD values underscore the stability of both the synthesized adsorbent and the analytical method employed.

Table 3. Removal efficiency of PhACs by Fe_3O_4@SB

PhACs	pH	Adsorbent dosage (mg)	Contact time (min)	Average removal (%)
MA	4	5	10	98.07
5-FU	8	5	15	96.53
TRP	6	5	10	98.27

Table 4. Intraday and inter-day precision of the adsorption method for PhACs using Fe_3O_4@SB

PhACs	Concentration (mg L^{-1})	Intraday RSD (%, n=5)	Interday RSD (%, n=5)
MA	5	1.27	1.23
5-FU	5	2.18	2.02
TRP	5	1.85	1.56

3.4. Factors influencing adsorption efficiency

The adsorption efficiency of the Fe_3O_4@SB nanocomposite for the target pharmaceutical compounds was evaluated as a function of key operational parameters: initial pH, contact time, and adsorbent dosage. The following sections detail the impact of each factor.

3.4.1. Effect of initial pH and the role of pHpzc

The solution pH is a critical parameter governing adsorption efficiency as it simultaneously influences the ionization state (speciation) of the pharmaceutical molecules and the surface charge of the Fe_3O_4@SB adsorbent. The experimentally determined pHpzc (~6.2) provides the essential reference point for a mechanistic interpretation of the observed trends (see Fig. 9) [39].

Mefenamic Acid (MA): Maximum adsorption occurred at pH 4. At this pH, which is below the pHpzc, the adsorbent surface is positively charged. MA, with a pK_a of approximately 4.2, exists primarily in its neutral molecular form at pH 4. Therefore, favorable electrostatic attraction can occur between the positively charged adsorbent surface and the anionic form of MA that is in equilibrium. Furthermore, the neutral

species interacts strongly via π-π stacking with the aromatic rings of the SB network and through hydrogen bonding (e.g., between MA's carboxyl group and non-protonated imine nitrogen on the adsorbent). The sharp decline in removal at pH < 4 is attributed to the excessive protonation of the adsorbent's functional groups, which diminishes their hydrogen-bonding capability, and the increased competition from H^+ ions [42, 43].

Tryptophan (TRP): The optimal removal was observed at pH 6, which is very close to the pHpzc. TRP is an amphoteric molecule with an isoelectric point (pI) of 5.9. At pH 6, TRP exists predominantly as a zwitterion with a net neutral charge (see Fig. 9). Simultaneously, the adsorbent surface is near its neutral point (pH ≈ pHpzc). This combination minimizes electrostatic repulsion, allowing the dominant adsorption mechanisms to proceed unhindered. These include multi-dentate hydrogen bonding involving TRP's amine and carboxylate groups and π-π interactions with its indole ring. At pH values significantly lower than the pI and pHpzc, both TRP (cationic) and the adsorbent (positively charged) experience electrostatic repulsion. At pH > pI, TRP becomes anionic, and the adsorbent surface also turns negative (pH > pHpzc), again leading to electrostatic repulsion and lower uptake [45].

5-Fluorouracil (5-FU): The highest adsorption was found at pH 8 (see Fig. 9). At this pH, which is above the pHpzc, the adsorbent surface carries a negative charge. 5-FU has a pK_a of about 8.0, meaning it is predominantly in its neutral molecular form at pH 8. Consequently, electrostatic repulsion is absent. The primary mechanism under this condition is hydrogen bonding, where the carbonyl and amine groups of 5-FU act as both donors and acceptors with the suitable sites (e.g., residual silanols, imine groups) on the adsorbent. Additionally, pore filling within the mesoporous SB network contributes to the uptake. The decrease in adsorption at pH > 8 occurs as 5-FU deprotonates to its anionic form, which may experience weak repulsion from the negatively charged surface and, more importantly, loses its ability to act as a strong hydrogen bond donor.

In summary, the adsorption performance is a direct consequence of the interplay between the adsorbent's pHpzc and the acid-base properties of the pharmaceuticals. The optimal pH for each compound represents a condition where either (a) favorable electrostatic attraction exists, or (b) electrostatic repulsion is minimized, thereby allowing stronger, non-electrostatic interactions (π-π stacking, hydrogen bonding) and pore filling to dominate the adsorption process.

The identified optimal pH values for the three pharmaceuticals (4, 6, and 8) align with the typical ranges reported for efficient removal of various drugs using engineered magnetic nanoparticles, which often achieve maximum performance at near-neutral conditions [44]. In summary, the adsorption performance of the Fe_3O_4@SB nanocomposite is a direct consequence of the interplay between the adsorbent's pHpzc and the acid-base properties of the pharmaceuticals, which dictates the speciation of the adsorbates and the surface chemistry of the adsorbent. The optimal pH for each pharmaceutical coincides with its dominant molecular or zwitterionic form, where key interactions such as π-π

stacking and hydrogen bonding are maximized, and electrostatic repulsion is minimized [45]. This pH-dependent mechanism is consistent with findings for other pollutant-adsorbent systems, including the chemical adsorption of anions onto amino-modified magnetic mesoporous materials [46]. A summary of the proposed adsorption mechanisms at the optimal pH for each compound is provided in Table 5.

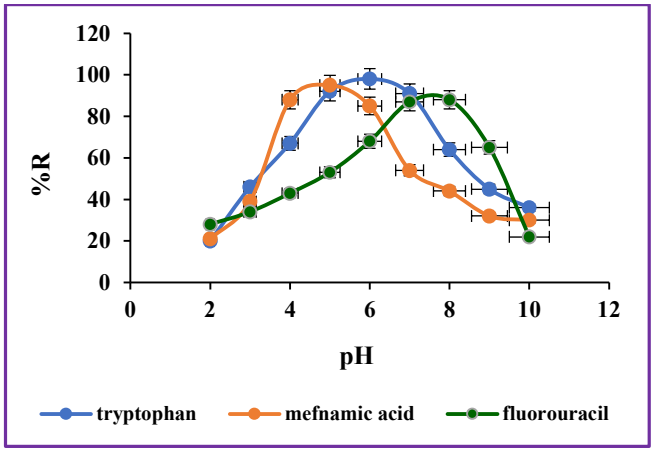

Figure 9. Effect of pH on the removal percentage of PhACs by Fe_3O_4@SB

Table 5. Proposed adsorption mechanisms for PhACs on Fe_3O_4@SB at their respective optimal pH conditions

Pharmaceutical compound	pH	Dominant species at optimal pH	Interaction mechanism
Mefenamic acid (MA)	4	Molecular ($pK_a \approx 4.2$)	**π-π Stacking & hydrogen bonding:** The molecular form of MA and the non-protonated imine groups on the adsorbent facilitate strong π-π interactions and hydrogen bonding.
Tryptophan (TRP)	6	Zwitterion (pI = 5.9)	**π-π Stacking & hydrogen bonding:** The zwitterionic form, with a net neutral charge, maximizes π-π interactions and multi-dentate hydrogen bonding, minimizing electrostatic repulsion.
5-Fluorouracil (5-FU)	8	Molecular ($pK_a \approx 8.0$)	**Hydrogen bonding & pore filling:** The molecular state preserves the ability of C=O and N-H groups to act as hydrogen bond donors/acceptors. Concurrently, the mesoporous structure allows for efficient physical entrapment.

3.4.2. Effect of contact time

The adsorption kinetics of the Fe_3O_4@SB nanocomposite were remarkably rapid, with equilibrium attained within 10 min for MA and TRP, and within 15 min for 5-FU (see Fig. 10). This fast kinetics is significantly quicker than many reported adsorbents, including other magnetic mesoporous materials used for drug loading which may take several hours to reach equilibrium [47], and is comparable to the performance of other advanced nanostructured Fe_3O_4 sorbents [48]. The effect of contact time on removal efficiency was investigated, a critical parameter for determining the equilibrium time and adsorption rate, as established in numerous adsorption studies [49]. The Fe_3O_4@SB nanocomposite's mesoporous structure and high concentration of surface functional groups, which enable quick diffusion and direct interaction with the target pharmaceutical chemicals, are responsible for the measured fast kinetics.

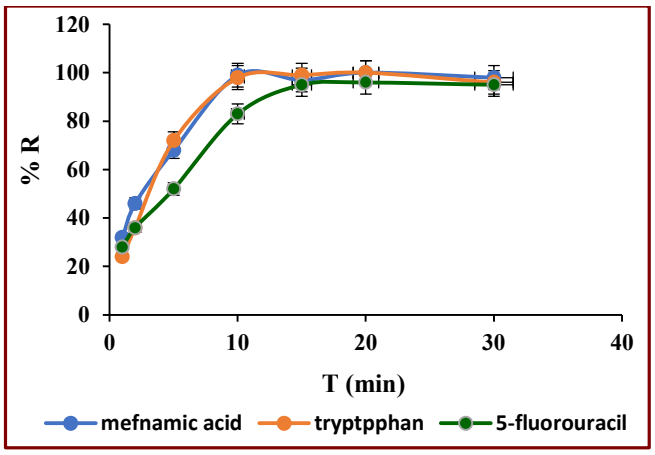

Figure 10. Effect of contact time on the removal percentage of PhACs by Fe_3O_4@SB

3.4.3. Effect of adsorbent dosage

The influence of adsorbent mass on the removal efficiency of the target analytes was systematically investigated, as this parameter is critical for assessing the practical and economic feasibility of the adsorption process [41, 50].

As the amount of adsorbent increased to 5 mg, the removal efficiency improved, but beyond that point, there was no discernible improvement (see Fig. 11). This plateau shows the achievement of saturation equilibrium, at which point adding more adsorbent has little effect, which is a typical finding in adsorption studies using similar magnetic nanomaterials. [51, 52]. The high efficiency achieved at a low optimal dosage of 5 mg underscores the operational efficiency of the nanocomposite and is comparable to the performance of other advanced magnetic adsorbents reported in the literature [53].

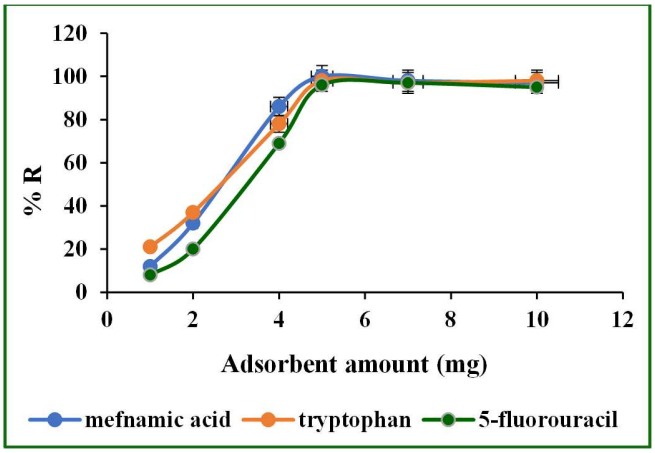

Figure 11. Effect of adsorbent dosage on the removal percentage of PhACs by Fe_3O_4@SB

3.5. Isotherms and kinetic models of adsorption

The equilibrium data were subsequently fitted to two fundamental adsorption isotherm models: Langmuir and Freundlich. The Langmuir model (Eq. 6) assumes monolayer adsorption onto a homogeneous surface with finite identical sites, while the Freundlich model (Eq. 7) describes multilayer adsorption on heterogeneous surfaces.

$$C_e/Q_e = 1/(Q_{max}\, K_L) + C_e/Q_{max} \quad (6)$$

$$\text{Ln}\, Q_e = \text{Ln}\, K_F + (1/n)\, \text{Ln}\, C_e \quad (7)$$

Where Q_{max} is the maximum monolayer adsorption capacity (mg g^{-1}), K_L is the Langmuir constant related to adsorption energy (L mg^{-1}), K_F represents the adsorption capacity (L mg^{-1}), and 1/n indicates adsorption intensity or surface heterogeneity.

The experimental equilibrium data were fitted to both the Langmuir and the Freundlich isotherm models to analyze the adsorption mechanism (see Fig. 12, and Table 6). The Freundlich model yielded higher correlation coefficients (R^2 = 0.996 – 0.998) compared to the Langmuir model (R^2 = 0.976 – 0.990), indicating that it provides a statistically better fit to the data across the studied concentration range. This is consistent with the expected heterogeneous nature of the Fe_3O_4@SB nanocomposite surface, which comprises a mixture of organic functional groups (e.g., imine, aromatic) and inorganic sites. The Freundlich intensity parameter 1/n values less than 1 (0.181 – 0.210) confirm a favorable adsorption process and the heterogeneity of the adsorbent surface [34].

Despite the superior statistical fit of the Freundlich model, the Langmuir model was also applied to estimate the apparent maximum monolayer adsorption capacity (Q_{max}), a standardized parameter crucial for comparing the saturation uptake of different adsorbents. The derived Qmax values were substantial: 175.45 mg g^{-1} for TRP, 172.41 mg g^{-1} for MA, and 151.50 mg g^{-1} for 5-FU [54-56]. The fact that the Langmuir model also provides a reasonably high correlation suggests that the adsorption data can be

approximated by a model of monolayer coverage, albeit on a surface with a distribution of site energies rather than identical sites. For a more nuanced description of the adsorption energy landscape on such composites, future analysis employing hybrid isotherms such as the Sips or Langmuir-Freundlich model would be valuable to quantify the heterogeneity factor.

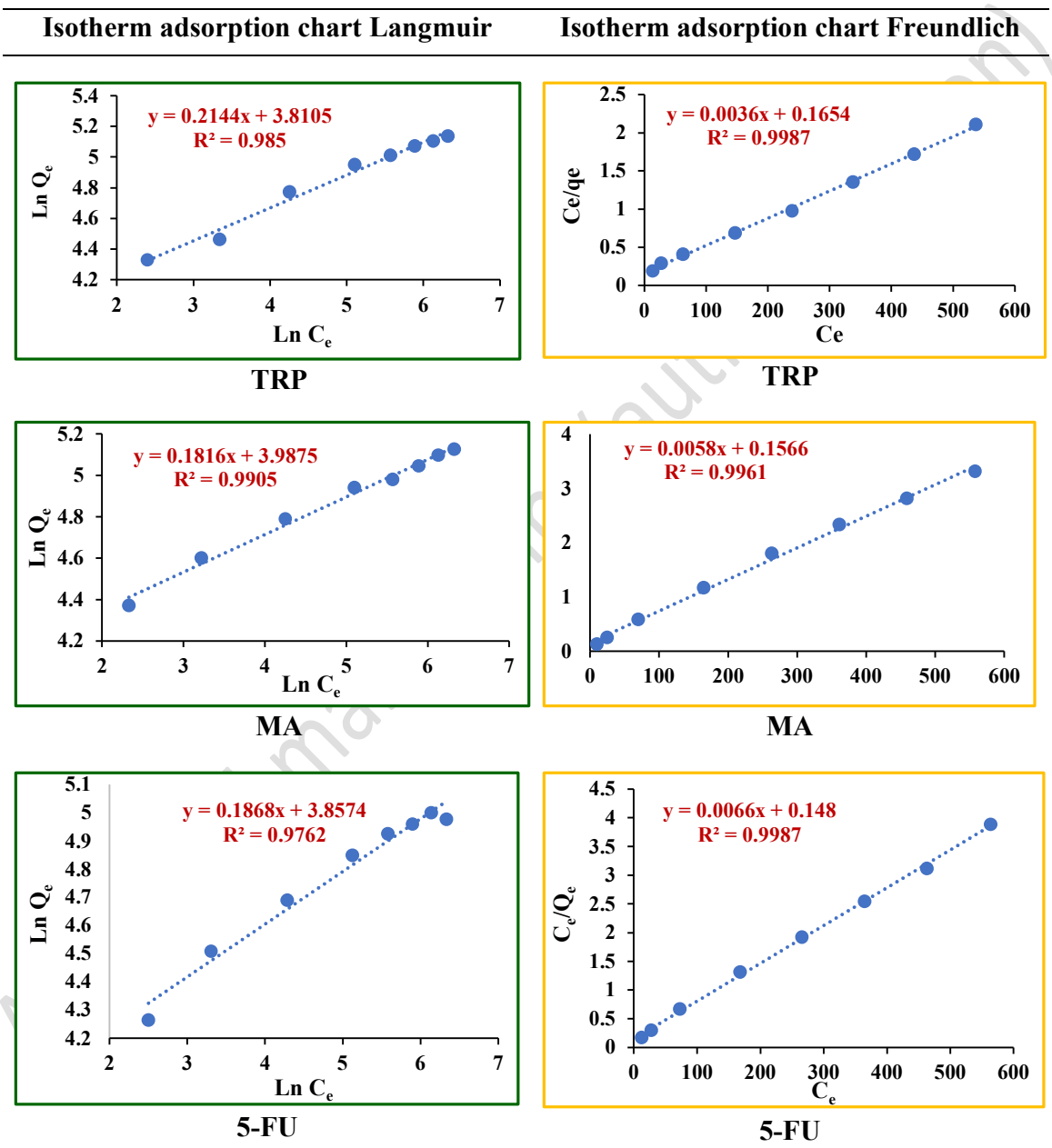

Figures 12. Langmuir and Freundlich adsorption isotherms for PhACs on Fe_3O_4@SB

Table 6. Langmuir and Freundlich adsorption isotherm parameters

PhACs	Langmuir parameters			Freundlich parameters		
	Q_{max} (mg g^{-1})	K_L (L mg^{-1})	R^2	K_F (L mg^{-1})	1/n	R^2
TRP	175.45	0.032	0.985	45.17	0.210	0.998
MA	172.41	0.037	0.990	53.91	0.181	0.996
5-FU	151.50	0.044	0.976	47.37	0.186	0.998

3.6. Comparative performance evaluation

The adsorption performance of the synthesized Fe_3O_4@SB nanocomposite was benchmarked against other magnetic Nano adsorbents reported in the literature for the removal of PhACs; the comparative data are compiled in Table 7. This analysis demonstrates that the Fe_3O_4@SB nanocomposite exhibits highly competitive and superior performance in several key aspects:

1. Rapid adsorption kinetics: The Fe_3O_4@SB achieves adsorption equilibrium within 10–15 min, which is significantly faster than many reported adsorbents, including metal-organic frameworks (MOFs) such as MIL-101-NH_2 (120 min). This rapid kinetics is attributed to the material's mesoporous structure, which facilitates swift diffusional mass transfer, and its abundant surface functional groups that provide readily accessible interaction sites.

2. High adsorption capacity: The nanocomposite exhibits high adsorption capacities for MA (172.41 mg g^{-1}), TRP (175.45 mg g^{-1}), and 5-FU (151.50 mg g^{-1}). While some specialized adsorbents report higher capacities for a single pollutant (e.g., 400 mg g^{-1} for ciprofloxacin on a complex composite), Fe_3O_4@SB maintains high efficacy across multiple pharmaceuticals with diverse chemical properties, underscoring its versatility.

3. Efficiency under practical conditions: The high removal efficiencies (>96%) were achieved with a low adsorbent dosage (5 mg) and at near-neutral pH for TRP (pH 6) and 5-FU (pH 8). This enhances its practical applicability for real water treatment scenarios, where minimal chemical adjustment and adsorbent use are economically favorable.

4. Favorable comparison with peer materials: When compared to other advanced magnetic COF composites (e.g., Fe_3O_4@COF for mycotoxins), the performance of Fe_3O_4@SB is comparable or superior, particularly in terms of its adsorption capacity for the target PhACs. Its performance surpasses that of simpler magnetic polymer/clay composites and functionalized activated carbons, which often exhibit slower kinetics.

In conclusion, this comparative analysis substantiates the claim that the novel Fe_3O_4@SB nanocomposite is a highly efficient, rapid, and versatile adsorbent. Its combination of properties positions it favorably among current state-of-the-art magnetic nano sorbents for the remediation of pharmaceutical contaminants in aqueous solutions.

Table 7. Comparative analysis of adsorption performance for PhACs removal

Adsorbent material	Target contaminant	Adsorption capacity (mg g^{-1})	Equilibrium time (min)	Optimal pH	Adsorption mechanism(s)	Reference
β-CD-functionalized magnetic clusters	Bisphenol A	52.7	30	7	Host-guest inclusion, H-bonding	[57]
Magnetic activated carbon	Sulfamethoxazole	104.5	1440 (24 h)	6	Pore filling, π-π EDA	[58]
Fe_3O_4/Chitosan/Polypyrrole	Cr(VI)	186.5	120	2	Electrostatic, reduction	[59]
Fe_3O_4@ZIF-67/$CuCo_2S_4$	Ciprofloxacin	400.0	90	6	Complexation, electrostatic	[60]
MIL-101-NH_2(Co/Fe)	5-FU	196.1	120	7	Electrostatic, π-π, H-bonding	[61]
Fe_3O_4@COF (TPA-HMD)	MA	243.9	5	4	Hydrogen bonding, π–π stacking, electrostatic attraction, hydrophobic interactions	[62]
	TRP	277.78	5	6	Hydrogen bonding, π–π stacking, electrostatic, hydrophobic interactions	
	5-FU	208.33	10	8	Hydrogen bonding, weak π–π stacking, pore filling	
Fe_3O_4@COF (TAPT-DHTA)	Aflatoxins, Zearalenone	125.8 - 185.2	~5	N/A	Hydrophobic, π-π, size exclusion	[18]
Fe_3O_4@SB	MA	172.41	10	4	π-π stacking, hydrogen bonding	This work
	TRP	175.45	10	6	π-π stacking,	

5-FU	151.50	15	8	hydrogen bonding Hydrogen bonding, pore filling

3.7. Adsorption mechanisms

The exceptional adsorption performance of the Fe_3O_4@SB nanocomposite arises from a synergistic combination of interactions between its functionalized surface and the target PhACs. The physicochemical properties of the adsorbent, confirmed by characterization, provide multiple complementary binding sites. The dominant mechanisms, π-π stacking, hydrogen bonding, and electrostatic interactions, are not mutually exclusive but operate in concert, with their relative contributions modulated by the solution pH, which dictates the ionization state of both the adsorbates and the adsorbent's functional groups (as informed by the pHpzc ≈ 6.2) (see Fig. 13).

1. *π-π Stacking interactions*: The Schiff base (SB) network, constructed from benzene-1,4-dicarboxaldehyde, provides an extended, electron-rich aromatic system. This creates an ideal platform for π-π interactions with the aromatic rings of MA (biphenyl moiety) and TRP (indole ring) [15]. For 5-FU, which lacks a traditional aromatic ring, interaction can occur through its conjugated double-bond system (pyrimidine ring) with the SB's aryl rings, representing a form of π-π interaction with an electron-deficient π-system [39]. This mechanism is largely pH-independent and provides a foundational, non-specific attraction.

2. *Hydrogen bonding (H-bonding)*: This is a primary, directional interaction that exploits the specific functional groups present on both the adsorbent and adsorbates.

- *Adsorbent sites*: The SB network offers imine (C=N) nitrogens as H-bond acceptors. Furthermore, unreacted amine groups from APTMS ($-NH_2$) and residual silanol groups (Si-OH) can act as both H-bond donors and acceptors [14].
- *Adsorbate interactions*:

MA: At optimal pH 4, MA is predominantly in its neutral, molecular form. Its carboxylic acid (-COOH) can act as a strong H-bond donor to the imine N and as an acceptor from amine/silanol groups. Concurrently, its secondary amine (-NH-) can donate a H-bond.

TRP: In its zwitterionic form at pH 6, TRP presents both a protonated ammonium ($-NH_3^+$) and a deprotonated carboxylate ($-COO^-$). The $-NH_3^+$ can engage in strong H-bond donation to imine N or silanol O, while the $-COO^-$ acts as an excellent H-bond acceptor from amine/silanol donors. Additionally, the indolic N-H is a potent H-bond donor.

5-FU: At pH 8, 5-FU is neutral, with both its amide-type N-H and carbonyl (C=O) groups available for H-bonding. It can form a complementary pair where its N-H donates to an imine N, and its C=O accepts from an amine/silanol donor [61].

The efficacy of H-bonding is highly pH-sensitive, as protonation or deprotonation of these groups can remove their ability to donate or accept H-bonds, explaining the sharp decline in efficiency at non-optimal pH values (see Fig. 9).

3. *Electrostatic interactions*: These become significant when the adsorbent surface and the adsorbate carry net charges. The pHpzc (≈6.2) is the key reference point.

- At pH < pHpzc, the adsorbent surface is positively charged (protonation of imine and amine groups).
- At pH > pHpzc, the surface becomes negatively charged (deprotonation of silanols and amines).

This surface charge interacts with the ionized forms of the PhACs: the anionic form of MA (pH > 4.2), the cationic form of TRP (pH < 2.4, for the amino group), the anionic form of TRP (pH > 9.4, for the carboxyl group), and the anionic form of 5-FU (pH > 8.0). Favorable electrostatic attraction enhances uptake (e.g., anionic MA at pH 4 with a positively charged surface), while electrostatic repulsion diminishes it (e.g., anionic 5-FU at pH >8 with a negatively charged surface) [17, 46]. The optimal pH for each PhAC represents a balance where repulsion is minimized, and other attractive forces are maximized.

4. *Pore filling and hydrophobic effect*: The mesoporous structure (avg. pore ~10.55 nm) provides a confined environment that enhances the local concentration of PhACs and facilitates multilayer interaction via the mechanisms above. Furthermore, the aromatic SB network and the hydrophobic moieties of the PhACs (especially MA and TRP) can engage in hydrophobic interactions, promoting their partitioning from the aqueous phase onto the adsorbent surface [62].

In summary, the adsorption is a multi-mechanistic process. For MA at pH 4, the primary drivers are π-π stacking with the biphenyl ring and H-bonding with the carboxyl group, aided by electrostatic attraction to the positively charged surface. For TRP at pH 6, adsorption is dominated by strong, multi-dentate H-bonding involving its zwitterionic groups and indolic N-H, coupled with π-π stacking of the indole ring, under conditions of net neutral surface charge. For 5-FU at pH 8, H-bonding is the principal mechanism, supplemented by weaker π-π interactions with the conjugated ring and pore filling, while operating on a negatively charged surface that does not cause significant repulsion against the neutral molecule.

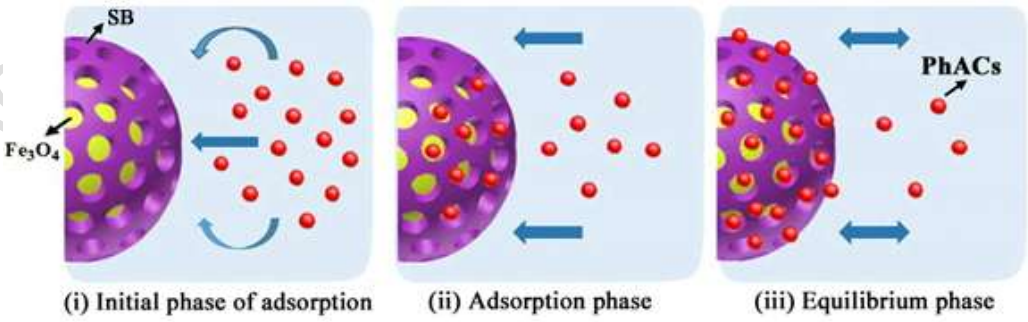

Figure 13. Proposed adsorption mechanisms of PhACs on Fe_3O_4@SB

3.8. Reusability of Fe_3O_4@SB

The reusability of the Fe_3O_4@SB nanocomposite was evaluated over five consecutive adsorption-desorption cycles. Methanol was selected due to its high desorption efficiency and frequent use in regeneration studies as a solvent. As shown in Fig. 14, the initial adsorption capacity for the PhACs was 209.8 ± 0.5 mg g^{-1}. A slight decrease in capacity was observed after each subsequent cycle, with the value reaching 199.1 ± 0.8 mg g^{-1} by the fifth cycle. This marginal decline of only 5.1% after five cycles demonstrates the high stability and excellent retention of adsorption capacity of the Fe_3O_4@SB adsorbent, a performance that aligns with recent studies on other advanced Fe_3O_4-based composites [63, 64]. The robust reusability is a key advantage of functionalized magnetic nanomaterials, as their facile magnetic separation prevents mass loss during recovery and their stable covalent functionalization, such as the Schiff base network in this work, ensures structural integrity over repeated use [65, 66]. This performance surpasses that of many comparable magnetic adsorbents [67, 68], and affirms the material's practical durability and economic viability for repeated applications in water treatment [69, 70].

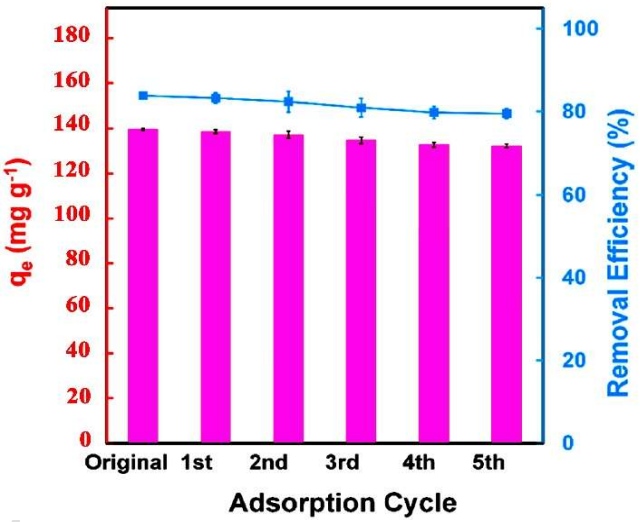

Figure 14. Reusability of the Fe_3O_4@SB nanocomposite

3.9. Future outlook of the Fe_3O_4@SB nanocomposite

This work presents a well-designed, efficient, and practical magnetic nanocomposite adsorbent for removing pharmaceutical active compounds (PhACs) from water. The demonstrated combination of high adsorption capacity, rapid kinetics, facile magnetic separation, and excellent reusability positions Fe_3O_4@SB as an auspicious material for water remediation. Building on these strong foundations, several compelling research directions and practical considerations emerge for future work:

1. Scalability and Green Synthesis
2. Expanded Pollutant Spectrum and Real-Water Matrices

3. Deepened Mechanistic Understanding and Material Optimization
4. Integration into Practical Treatment Systems
5. Long-Term Stability and Environmental Impact Assessment
6. Functional Diversification

The development of Fe_3O_4@SB is a significant contribution to the field of magnetic Nano adsorbents. Its future impact will be determined by successfully transitioning from a high-performing lab-scale material to a scalable, cost-effective, and integrated component of water treatment technologies. Addressing the outlined directions, particularly scalability, performance in real matrices, system integration, and thorough environmental assessment, will be essential to bridge the gap between promising academic research and tangible environmental remediation solutions. This work provides a robust platform upon which the next generation of intelligent, multifunctional, and sustainable water treatment materials can be built.

4. Conclusion

This study successfully demonstrates the design, synthesis, and application of a novel magnetic mesoporous nanocomposite, Fe_3O_4@SB, for the highly efficient removal of PhACs from aqueous solutions. The nanocomposite was fabricated through a sequential process involving the co-precipitation of a superparamagnetic Fe_3O_4 core, its functionalization with APTMS, and subsequent growth of a Schiff base network via condensation with BDC. Comprehensive characterization by FT-IR, XRD, VSM, SEM, EDX, and BET analyses confirmed the successful covalent functionalization, superparamagnetic properties (M_s = 30 emu g^{-1}), mesoporous architecture, and robust crystalline structure.

The Fe_3O_4@SB nanocomposite exhibited exceptional adsorption performance for three model PhACs with distinct physicochemical properties: MA, TRP, and 5-FU. Under optimized conditions, the adsorbent achieved remarkable removal efficiencies exceeding 96% for all compounds. A key advantage is the remarkably rapid adsorption kinetics, with equilibrium attained within 10–15 min, which is attributed to the material's mesoporous structure and abundant surface functional groups that facilitate swift diffusion and interaction. Adsorption isotherm analysis revealed that the process was best described by the Langmuir model, indicating monolayer adsorption on a homogeneous surface. The maximum adsorption capacities were high, reaching 172.41 mg g^{-1} for MA, 175.45 mg g^{-1} for TRP, and 151.50 mg g^{-1} for 5-FU. The dominant mechanisms governing the adsorption were identified as π-π stacking and hydrogen bonding, the efficacy of which was highly dependent on the solution pH and the ionization state of both the adsorbates and the adsorbent's functional groups.

Furthermore, the Fe_3O_4@SB nanocomposite demonstrated excellent reusability and stability over five consecutive adsorption-desorption cycles with only a minimal loss in performance, underscoring its practical and economic viability for repeated use. The combination of facile synthesis, high adsorption capacity, rapid kinetics, efficient

magnetic separability, and robust reusability positions Fe_3O_4@SB as a highly promising and versatile adsorbent. This work effectively bridges the gap between high-performance material design and operational practicality, offering a sustainable and efficient solution for the remediation of pharmaceutical-contaminated water streams.

While the Fe_3O_4@SB nanocomposite demonstrated excellent structural stability over multiple cycles, future studies will focus on comprehensive environmental safety assessments. This includes rigorous leaching tests for iron ions and organic components, as well as ecotoxicity bioassays, to ensure no secondary contamination occurs during the water treatment process and to fully validate its environmental compatibility.

Acknowledgment

The authors are grateful to the Islamic Azad University, Rasht Branch, and the Islamic Azad University, Ardabil Branch.

Authors contributions

Authors have contributed equally in preparing and writing the manuscript.

Availability of data and materials

The data that support the findings of this study are available from the corresponding author upon reasonable request.

Conflict of interest

The authors declare that they have no known competing financial interests or personal relationships that could have appeared to influence the work reported in this paper.

References

[1] C.F. Couto, L.C. Lange, M.C. Amaral, J. Water Process Eng. 32 (2019) 100927. https://doi.org/10.1016/j.jwpe.2019.100927.

[2] M.A. Vaudreuil, S.V. Duy, G. Munoz, S. Sauvé, Sci. Total Environ. 846 (2022) 157353. https://doi.org/10.1016/j.scitotenv.2022.157353.

[3] A. Majumder, B. Gupta, A.K. Gupta, Environ. Res. 176 (2019) 108542. https://doi.org/10.1016/j.envres.2019.108542.

[4] B.A. Otoo, I.A. Amoabeng, G. Darko, L.S. Borquaye, Toxicol. Rep. 9 (2022) 1491–1500. https://doi.org/10.1016/j.toxrep.2022.07.003.

[5] L.O. Omuferen, B. Maseko, J.O. Olowoyo, Environ. Monit. Assess. 194 (2022) 306. https://doi.org/10.1007/s10661-022-09846-4.

[6] M. Jalilian, P. Parvizi, M.R. Zangeneh, Water Environ. Res. 97 (2025) e70062. https://doi.org/10.1002/wer.70062.

[7] M.D. Nguyen, H.V. Tran, S. Xu, T.R. Lee, Appl. Sci. 11 (2021) 11301. https://doi.org/10.3390/app112311301.

[8] V. Singh, Corros. Manag. 34 (2024) 141–162. https://doi.org/10.3390/4asxce56.

[9] R. Shekhanavar, S. Khatavi, B.G. Hegde, K. Kantharaju, Iran. J. Catal. 15 (2025). https://doi.org/10.57647/j.ijc.2025.1502.17.

[10] N. Zekri, R. Fareghi-Alamdari, Iran. J. Catal. 14 (2024). https://doi.org/10.57647/j.ijc.2024.1401.02.
[11] S.P. Schwaminger, C. Syhr, S. Berensmeier, Crystals 10 (2020) 214. https://doi.org/10.3390/cryst10030214.
[12] A.P. Côté, A.I. Benin, N.W. Ockwig, M. O'Keeffe, A.J. Matzger, O.M. Yaghi, Science 310 (2005) 1166–1170. https://doi.org/10.1126/science.1120411.
[13] Y. Ma, X. Kuang, X. Deng, B. Zi, J. Zeng, J. Zhang, Z. Zhu, Y. Zhang, Q. Liu, Microporous Mesoporous Mater. 335 (2022) 111701. https://doi.org/10.1016/j.micromeso.2022.111701.
[14] J.L. Segura, M.J. Mancheño, F. Zamora, Chem. Soc. Rev. 45 (2016) 5635–5671. https://doi.org/10.1039/C5CS00878F.
[15] G. Lin, C. Gao, Q. Zheng, Z. Lei, H. Geng, Z. Lin, H. Yang, Z. Cai, Chem. Commun. 53 (2017) 3649–3652. https://doi.org/10.1039/C7CC00482F.
[16] M. Moharramnejad, T. Sayah, Z. Ghehsareh, M.M. Rezaei, A.H. Amini, R.E. Malekshah, M. Shahi, B. Mirtamizdoust, A. Ehsani, J. Haribabu, S.C. Hsu, J. Drug Delivery Sci. Technol. 102 (2024) 106320. https://doi.org/10.1016/j.jddst.2024.106320.
[17] L. You, K. Xu, G. Ding, X. Shi, J. Li, S. Wang, J. Wang, J. Mol. Liq. 320 (2020) 114456. https://doi.org/10.1016/j.molliq.2020.114456.
[18] J. Wang, Q. Huang, W. Guo, D. Guo, Z. Han, D. Nie, Toxins 15 (2023) 117. https://doi.org/10.3390/toxins15020117.
[19] H. Zhang, W. Ma, C. Qiang, J. Nie, L. Ma, Y. Zhang, K. Wang, RSC Adv. 15 (2025) 8111–8120. https://doi.org/10.1039/D5RA00811E.
[20] D. Kirubakaran, J.B. Wahid, N. Karmegam, R. Jeevika, L. Sellapillai, M. Rajkumar, K.J. SenthilKumar, Biomed. Mater. Devices (2025) 1–26. https://doi.org/10.1007/s44174-025-00295-4.
[21] S.I.A.R. Shah, W. Ahmad, M. Anwar, R. Shah, J.A. Khan, N.S. Shah, A. Al-Anazi, C. Han, Appl. Catal. O Open (2025) 207049. https://doi.org/10.1016/j.apcato.2025.207049.
[22] W. Wu et al., Adv. Mater. Interfaces 9 (2022) 2201423. https://doi.org/10.1002/admi.202201423.
[23] N. Omrani, A. Nezamzadeh-Ejhieh, M. Alizadeh, Desalin. Water Treat. 162 (2019) 290–302. https://doi.org/10.5004/dwt.2019.24352.
[24] L. You, K. Xu, G. Ding, X. Shi, J. Li, S. Wang, J. Wang, J. Mol. Liq. 320 (2020) 114456. https://doi.org/10.1016/j.molliq.2020.114456.
[25] M. Al-Kelani, N. Buthelezi, Skin Res. Technol. 30 (2024) e13733. https://doi.org/10.1111/srt.13733.
[26] W. Wu, Z. Wu, T. Yu, C. Jiang, W.S. Kim, Sci. Technol. Adv. Mater. 24 (2023) 2153431. https://doi.org/10.1088/1468-6996/16/2/023501.
[27] S.R. Ansari, J. Mahajan, A. Teleki, WIREs Nanomed. Nanobiotechnol. 16 (2024) e1963. https://doi.org/10.1002/wnan.1963.
[28] J.E. Ogbezode, U.S. Ezealigo, A. Bello, V.C. Anye, A.P. Onwualu, Discover Nano 18 (2023) 125. https://doi.org/10.1186/s11671-023-03898-2.
[29] S.G. Hasan, A.V. Gupta, B.V. Reddi, Mater. Today Proc. 47 (2021) 4137–4141. https://doi.org/10.1016/j.matpr.2021.08.146.
[30] H. Quanguo, Z. Lei, W. Wei, H. Rong, H. Jingke, Sens. Mater. 22 (2010) 285–295. https://doi.org/10.18494/SAM.2010.622.

[31] M.S. Sharif, H. Hameed, A. Waheed, M. Tariq, A. Afreen, A. Kamal, E.A. Mahmoud, H.O. Elansary, S. Saqib, W. Zaman, Molecules 28 (2023) 3403. https://doi.org/10.3390/molecules28083403.
[32] S. Bassim, A.K. Mageed, A.A. AbdulRazak, H.S. Majdi, Inorganics 10 (2022) 260. https://doi.org/10.3390/inorganics10120260.
[33] B. Mashhourzad, B. Zeynizadeh, Nanoscale Adv. (2025). https://doi.org/10.1039/D4NA01020E.
[34] J. Villarroel-Rocha, D. Barrera, K. Sapag, Microporous Mesoporous Mater. 200 (2014) 68–78. https://doi.org/10.1016/j.micromeso.2014.08.017.
[35] S. Sani, R. Adnan, W.D. Oh, A. Iqbal, Nanomaterials 11 (2021) 2742. https://doi.org/10.3390/nano11102742.
[36] J. Tom, Last accessed March 3, 2021 (2022) [Incomplete source].
[37] M. Liu, Appl. Comput. Eng. 159 (2025) 85–92. https://www.ewadirect.com/proceedings/ace/article/view/23761.
[38] V. Dharmawan, I. Rahmawati, A.R. Sanjaya, B.E. Dewi, E. Saepudin, T.A. Ivandini, Int. J. Technol. 16 (2025) 672–685. https://doi.org/10.14716/ijtech.v16i2.7176.
[39] Q. Wang, G. Wang, S. Xie, X. Zhao, Y. Zhang, Exp. Ther. Med. 17 (2019) 2694–2702. https://doi.org/10.3892/etm.2019.7238.
[40] S. Abolghasemi, A.R. Nasiri, M. Hashemi, S. Rajabi, F. Rahimi, Appl. Water Sci. 15 (2025) 1–54. https://doi.org/10.1007/s13201-025-02360-1.
[41] M. Sun, X. Bai, X. Fu, X. Yu, Z. Ye, M. Zhang, Y. Qiu, Sci. Rep. 15 (2025) 4751. https://doi.org/10.1038/s41598-025-87901-z.
[42] A.A. Siyal, R.M. Mohamed, F. Ahmad, M.A. Malek, M. Alsubih, R. Shamsuddin, S. Hussain, S. Musa, RSC Adv. 15 (2025) 17843–17861. https://doi.org/10.1039/D5RA02007G.
[43] S. Siratham, K. Osathaphan, P. Punyapalakul, Sci. Rep. 15 (2025) 34454. https://doi.org/10.1038/s41598-025-17629-3.
[44] L.Y. George, L. Ma, W. Zhang, G. Yao, Environ. Sci. Eur. 35 (2023) 21. https://doi.org/10.1186/s12302-023-00725-4.
[45] R. Öztekin, D.T. Sponza, Clin. Trials Clin. Res. 3 (2024). https://doi.org/10.31579/2834-5126/068.
[46] S.K. Pereira, S. Kini, B. Prabhu, G.P. Jeppu, Appl. Water Sci. 13 (2023) 29. https://doi.org/10.1007/s13201-022-01800-6.
[47] A. Gençer, B.U. Karataş, Ö. Topel, N. Kiraz, Turk. J. Chem. 48 (2024) 50–64. https://doi.org/10.55730/1300-0527.3638.
[48] A.M. Alkafajy, T.M. Albayati, Mater. Today Commun. 23 (2020) 100890. https://doi.org/10.1016/j.mtcomm.2019.100890.
[49] S.H. Yu, Y. Wang, Y.Y. Wan, J.K. Guo, Environ. Sci. Pollut. Res. 30 (2023) 94401–94413. https://doi.org/10.1007/s11356-023-29060-0.
[50] A.J. Jafari, B. Kakavandi, R.R. Kalantary, H. Gharibi, A. Asadi, A. Azari, A.A. Babaei, A. Takdastan, Korean J. Chem. Eng. 33 (2016) 2878–2890. https://doi.org/10.1007/s11814-016-0155-x.
[51] O. Reyes-Vallejo, R.M. Sánchez-Albores, J. Escorcia-García, A. Cruz-Salomón, P. Bartolo-Pérez, A. Adhikari, M. del Carmen Hernández-Cruz, H.H. Torres-Ventura, H.A. Esquinca-Avilés, Environ. Sci. Pollut. Res. 32 (2025) 1–25. https://doi.org/10.1007/s11356-025-36310-w.

[52] A.H. Al-Mahfuz, A. Ghaemi, J. Environ. Eng. Sci. 19 (2024) 206–213. https://doi.org/10.1680/jenes.23.00096.
[53] Y. Liu, M. Yao, Z. Jin, Y. Zhang, npj Clean Water 8 (2025) 40. https://doi.org/10.1038/s41545-025-00453-7.
[54] R. Mirbagheri, D. Elhamifar, M. Shaker, Sci. Rep. 11 (2021) 23259. https://doi.org/10.1038/s41598-021-02699-w.
[55] A. El-Denglawey, M.F. Mubarak, H. Selim, Arab. J. Sci. Eng. 47 (2022) 455–476. https://doi.org/10.1007/s13369-021-05690-9.
[56] A. El Jery, H.S. Alawamleh, M.H. Sami, H.A. Abbas, S.S. Sammen, A. Ahsan, M. Imteaz, A.A. Shanableh, M. Shafiquzzaman, H. Osman, N. Al-Ansari, Sci. Rep. 14 (2024) 970. https://doi.org/10.1038/s41598-023-50937-0.
[57] M. Kanagalakshmi, S.G. Devi, P. Ananthi, A. Pius, in: Carbon Nanomater. Their Compos. Adsorb., Springer, 2024, pp. 135–154. https://doi.org/10.1007/978-3-031-48719-4-8.
[58] J.H. Lee, S.Y. Kwak, Appl. Surf. Sci. 467 (2019) 178–184. https://doi.org/10.1016/j.apsusc.2018.10.054.
[59] M. Lv, D. Li, Z. Zhang, B.E. Logan, G. Liu, M. Sun, C. Dai, Y. Feng, Sci. Total Environ. 757 (2021) 143717. https://doi.org/10.1016/j.scitotenv.2020.143717.
[60] L. Yin, K. Wang, L. Jiang, Y. Xi, Z. Xu, Z. Song, H. Zhou, RSC Adv. 15 (2025) 16337–16347. https://doi.org/10.1039/D5RA00872G.
[61] M.A. Diab, A.B. Ali, A. Abdulrahman, A. BaQais, M.I. Khan, A. Abduvokhidov, M. Karimov, O. Mukhitdinov, I. Mahariq, Surf. Interfaces 73 (2025) 107517. https://doi.org/10.1016/j.surfin.2025.107517.
[62] L.R. Rad, H. Faramarzi, M. Anbia, M. Irani, Sep. Purif. Technol. 339 (2024) 126597. https://doi.org/10.1016/j.seppur.2024.126597.
[63] S. Shenavaie asl, A. Pourahmad, S.R. Mansour, N. Sohrabi-Gilani, Results Chem. (2025) 102876. https://doi.org/10.1016/j.rechem.2025.102876.
[64] D. Ramutshatsha-Makhwedzha, M.L. Mavhungu, J. Baloyi, R. Mbaya, J. Iran. Chem. Soc. 22 (2025) 113–128. https://doi.org/10.1007/s13738-024-03135-2.
[65] M. Shaker, D. Elhamifar, New J. Chem. 44 (2020) 3445–3454. https://doi.org/10.1039/C9NJ06250E.
[66] S. Simsek, H.I. Ulusoy, J. Polym. Environ. 26 (2018) 1605–1612. https://doi.org/10.1007/s10924-017-1067-5.
[67] J.H. Lee, S.Y. Kwak, Appl. Surf. Sci. 467 (2019) 178–184. https://doi.org/10.1016/j.apsusc.2018.10.054.
[68] I.K. Rind, M.F. Lanjwani, A. Sarı, M. Tuzen, T.A. Saleh, Nano-Struct. Nano-Objects 39 (2024) 101283. https://doi.org/10.1016/j.nanoso.2024.101283.
[69] D. Chen, T. Awut, B. Liu, Y. Ma, T. Wang, I. Nurulla, e-Polymers 16 (2016) 313–322. https://doi.org/10.1515/epoly-2016-0043.
[70] Z. Heidarnezhad, A. Ghorbani-Choghamarani, Z. Taherinia, Nanoscale Adv. 6 (2024) 4360–4368. https://doi.org/10.1039/D4NA00414K.